



ACADÉMIE
DES SCIENCES
INSTITUT DE FRANCE

Comptes Rendus

Mécanique


Mehdi Boudouh, Brahim Elkhail Hachi, Boulanouar Azzouzi, Bassem Zouari
and Mohamed Haboussi

**Crack propagation in concrete mortar under quasi-static tensile loading:
experimental insights and phase-field modeling**

Volume 353 (2025), p. 1225-1260

Online since: 24 November 2025

<https://doi.org/10.5802/crmeca.338>

 This article is licensed under the
CREATIVE COMMONS ATTRIBUTION 4.0 INTERNATIONAL LICENSE.
<http://creativecommons.org/licenses/by/4.0/>



*The Comptes Rendus. Mécanique are a member of the
Mersenne Center for open scientific publishing*
www.centre-mersenne.org — e-ISSN : 1873-7234



Research article

Crack propagation in concrete mortar under quasi-static tensile loading: experimental insights and phase-field modeling

Mehdi Boudouh^{*,a}, Brahim Elkhailil Hachi^a, Boulanouar Azzouzi^a,
Bassem Zouari^b and Mohamed Haboussi^c

^a Laboratory of Development in Mechanics and Materials (LDMM), University of Djelfa, PB 3117, Djelfa, Algeria

^b LA2MP Laboratory, National Engineering School of Sfax, University of Sfax, Sfax 3029, Tunisia

^c Laboratoire LSPM Université Sorbonne Paris Nord UPR 3407 CNRS, 93430, Villeteuse, France

E-mail: mehdi.boudouh@univ-djelfa.dz (M. Boudouh)

Abstract. This study investigates crack propagation in concrete mortar under quasi-static tensile loading with imposed displacement. Several rectangular cubic concrete specimens containing a predefined crack and hole were cast and tested. The load–displacement curves and crack paths were obtained experimentally and analyzed, enabling us to assess the influence of the specimen age parameter on fracture behavior. The evolution of mechanical properties as a function of age, in particular the modulus of elasticity E and Poisson's ratio ν (characterized by ultrasonic testing), was monitored. The fracture energy G_c was determined by direct tensile testing. These parameters were fed into a phase field model implemented by the finite element method in a computational code developed in MATLAB®. The solution is based on a variational system that treats the displacement and damage fields in an alternating minimization scheme. The numerical results were compared in two distinct frameworks: one in a logical domain and the other in a physical domain. Finally, the results obtained in each of these frameworks were compared with experimental results, revealing relatively good agreement.

Keywords. Direct tensile tests, Material characterization, Phase field model, Crack propagation, Alternated minimization, Finite element Methode.

Manuscript received 25 April 2025, revised 27 September 2025, accepted 28 October 2025.

1. Introduction

Concrete plays a key role in engineering structures due to its exceptional compressive strength and remarkable durability under various environmental conditions. Despite these advantages, which make it a popular choice among engineers and architects, concrete has two notable drawbacks that can impact its overall performance: its relatively low tensile strength and inherent brittleness. These properties lead to cracking, which is one of the primary failure mechanisms observed in nearly all brittle cementitious materials [1,2].

In 1961, Kaplan [3] conducted a series of experimental fracture tests on concrete beams, applying Griffith's theory [4] to better understand the complex behavior of cracks and fractures

*Corresponding author

in solid materials. This work marked the systematic introduction and development of fracture mechanics and damage mechanics, providing a rigorous framework for analyzing the non-linear properties of concrete materials.

Bruhwieler et al. [5], performed a series of wedge-splitting tests on concrete specimens with predefined cracks. They observed that fracture toughness values remained unaffected by crack size, demonstrating that the fracture behavior of concrete remained consistent despite variations in crack dimensions.

Zhang et al. [6] evaluated concrete toughness through wedge-splitting tests and applied several analytical techniques, including the simplified Green's function method, the simplified equivalent cohesive force method, the four-term weighting function method, and the Gauss-Chebyshev integral method. Their findings revealed a strong agreement between the results of the wedge-splitting tests and those obtained from each of the four analytical approaches. Xu et al. [7] developed a numerical method to derive the stress-strain curve of concrete, incorporating the fracture process zone observed during three-point bending tests.

Landis [8] investigated micro-macro fracture relationships in concrete using Acoustic Emission (AE) and found that AE activity increases sharply at the onset of microcracking, and that the spatial distribution of AE sources predicts the eventual macrocrack trajectory. To get more information about crack initiation and propagation, Dai et al. [9], Alam et al. [10], Rouchier et al. [11], Verbruggen et al. [12], Sharma et al. [13] conducted an extensive study on the fracture process zone (FPZ) in concrete employing both digital image correlation (DIC) and acoustic emission (AE). They showed that AE could detect and localize the initiation of microcracks within the specimen volume, while DIC provided full-field strain and displacement measurements on the surface, enabling accurate tracking of FPZ development.

Zhang et al. [14] conducted an extensive study to capture crack initiation, using the acoustic emission (AE) technique as a key analytical tool, particularly during three-point bending tests on concrete specimens with predefined cracks. Fang et al. [15] evaluated the performance characteristics related to the early crack resistance of concrete, focusing on mixtures containing ternary mineral components, using a thermal stress testing machine.

Guan et al. [16] conducted a series of wedge splitting tests on solid concrete specimens and found a significant correlation between the age of the concrete and its mechanical properties, specifically noting that toughness and fracture energy increased as the concrete aged. Refs. [17,18] conducted wedge splitting tests on solid concrete specimens with predefined cracks and found that specimens cast during the summer months exhibited higher fracture energy values than those cast in the winter months. In addition, Xu et al. [19] conducted a detailed examination and found that toughness and fracture energy were largely unaffected by changes in the predefined crack length. Meanwhile, Wittmann et al. [20] conducted rigorous evaluations to determine the fracture parameters of concrete using the tensile test, Chen et al. [21] investigated the tensile properties of concrete under high strain rates using the split Hopkinson pressure bar technique.

Due to the challenges and complexities of conducting direct experimental tensile tests on concrete materials, researchers often turn to indirect methods as practical alternatives to effectively study the tensile behavior of concrete Zheng et al., Mesbah et al. [22,23]. Among the various indirect testing methods introduced in the field is the Brazilian disc test, developed by Rocco et al. [24], four-point bending tests by Wu et al. [7], and the three-point bending test by Lok et al. [25]. In addition, research conducted by Lok et al., Ruiz et al. [25,26] involved performing splitting tensile tests using the split Hopkinson pressure bar (SHPB).

A considerable body of research has focused on the tensile response of concrete using direct tension tests, despite the inherent experimental difficulties associated with such methods. Van Mier and Van Vliet [27] provided a comprehensive review of direct tension testing techniques,

identifying critical issues such as eccentricity, secondary bending, and platen misalignment, and demonstrated the necessity of servo-controlled systems to obtain reliable measurements of tensile strength and fracture energy. Earlier, Reinhardt and Cornelissen [28] conducted deformation-controlled uniaxial tension tests under both static and cyclic loading on lightweight and normal-weight concretes. Their results emphasized the significance of post-peak softening behavior and yielded essential data for constitutive model development under monotonic and cyclic load conditions. More recently, Nouailletas et al. [29] performed cyclic tension–compression tests on notched specimens, combining traditional displacement sensors with digital image correlation (DIC). Their findings revealed that crack closure under compression partially restored stiffness, while frictional interactions along crack faces substantially contributed to inelastic strain and energy dissipation.

To address persistent experimental limitations, several improved testing protocols have been introduced. Alhussainy et al. [30] proposed an innovative specimen geometry incorporating a reduced cross-section and universal grips, ensuring systematic midspan failure without slippage and thereby enabling reproducible stress–strain characterization. In a related study, Alhussainy et al. [31] examined the direct tensile behavior of self-consolidating concrete (SCC) using specially designed metallic grips. Their experiments confirmed consistent fracture initiation at the specimen midsection and showed that direct tensile strength values were systematically lower than those obtained from indirect methods such as Brazilian or flexural testing.

The mechanical response of concrete is governed not only by its inherent heterogeneity arising from aggregate distribution, cement matrix properties, and interfacial transition zones, but also by its geometric configuration. The presence of initial defects (cracks, voids, notches) or geometric discontinuities (section reductions, eccentricities) modifies stress distribution and apparent stiffness, thereby influencing crack initiation, propagation, and overall resistance. Moreover, the age of the material is a decisive parameter, as the progressive evolution of mechanical properties directly impacts structural performance under load. This complexity highlights the need to accurately characterize the mechanical parameters governing the stiffness and deformation capacity of concrete. The estimation of Young's modulus and Poisson's ratio has been the subject of numerous studies, using both destructive and non-destructive approaches. Compression or bending tests remain the traditional method for determining the static modulus E_s , but they depend on experimental conditions and involve the destruction of test specimens [32–34]. To overcome these limitations, non-destructive methods, particularly ultrasound, have been developed. As early as the 1990s, Boumiz et al. [35] and Martin et al. [36] demonstrated the relevance of P and S wave velocities for characterizing hydration and elastic properties, while more recent work [35,37] have confirmed their effectiveness in monitoring setting and correlation with strength. Finally, several studies [33,34,38,39] have established relationships between static and dynamic modules, confirming the complementary nature of the approaches: static tests provide references, while ultrasound allows for continuous, non-destructive monitoring.

While experimental testing provides invaluable insights, it is often time-consuming, costly, and limited in scope. Consequently, numerical modeling has become a cornerstone of fracture research. A predominant feature of most numerical models is their tendency to bypass the singularities that appear in displacement fields as a result of crack formation in structures. Various numerical methods for simulating crack initiation and propagation have been founded and developed in recent years. These methods can be classified into two main types, called discrete crack models and diffuse crack models. In discrete crack models, it is assumed that damage within the material is concentrated on an exceptionally short length scale, allowing localized analysis of crack behavior. Many researchers have used discrete crack models for crack growth and propagation in solids. Examples include [40,41] in the case of the brutal fracture and [42–46] in the case of fatigue.

Diffuse crack models conceptualize the crack phenomenon as a zone of damage distributed over a finite volume. These models are widely adopted due to their relatively simple implementation in a calculation code and their ability to handle complex crack configurations. Rather than considering discrete cracks, these models are based on a diffuse approximation that incorporates the effects of crack formation. The phase field model belongs to this class of diffuse cracking models; it extends Griffith's theory by simultaneously determining the displacement field and the crack trajectory by minimizing the total potential energy in a variational framework [47,48]. Bourdin et al. [49,50] have established the fundamental principles for the numerical implementation of this approach. A damage phase field is introduced to transform a clean crack into a regularized damage band, whose width is controlled by a characteristic scaling parameter.

A central feature of phase-field fracture models is the introduction of an internal length scale ℓ , which governs the thickness of the diffused crack and ensures the well-posedness of the variational formulation. Several strategies have been proposed for its calibration. Early works [51,52] suggested experimental identification or calibration through size-effect tests, though Iacono et al. [53] showed that this procedure does not lead to a unique solution. Later studies [54–56] interpreted ℓ as a material parameter, intrinsically linked to the tensile strength of a homogeneous medium. More recently, Nguyen et al. [57], and Li et al. [58] emphasized the need to ensure consistency between ℓ and the microstructural heterogeneity of cementitious composites. In particular, mesoscale analyses of concrete and mortar have shown that ℓ should be related to the characteristic size of sand grains or aggregates in order to retain physical representativity [58,59]. At the same time, Miehe et al. [60], Farrell and Maurini [61] highlighted that ℓ also influences numerical stability, conditioning, and convergence of the finite element solution. Therefore, the choice of ℓ must balance physical consistency with computational robustness, a point that is especially critical when modelling granular quasi-brittle materials such as concrete.

In addition to the phase-field approach, several other continuous regularized methods have been proposed in the literature to address the challenges related to crack initiation, propagation, and localization in quasi-brittle materials. Nonlocal models, of gradient or integral type [55,62,63], introduce an internal length scale that makes it possible to account for size effects observed in concrete structures. The Thick Level Set (TLS) method [64–66] combines a local damage law with an imposed localization profile, enabling a natural representation of crack initiation, coalescence, and branching. More recently, the Lip-field approach [67–69] has been proposed as a mathematically rigorous regularization technique, ensuring boundedness of the damage gradient through a Lipschitz continuity constraint. These phase field models share a common point: the introduction of an internal length ℓ that regularizes the damage field and provides a physically consistent description of fracture in quasi-brittle media. In comparison with these methods, the phase field model also takes into account the size effect while offering a numerically inexpensive formalism given its well-established variational form with remarkable simplicity in the treatment of nucleation and crack branching. All of this led us to choose the phase field approach as our modeling method.

The numerical implementation of phase field models is generally carried out within the framework of the finite element method (FEM), due to the fact that the equations governing these models are partial differential equations, which can be solved efficiently using this approach. The spatial discretization of the domain using finite elements can be implemented relatively simply. Numerous studies have documented finite element implementations of phase field models, including the work of Amor et al. [54], Bourdin et al. [70], Lee et al. [71], Miehe et al. [72], Sargado et al. [73], Wu [74], Kriaa et al. [75], Piska et al. [76], Yuanfeng et al. [77], Hachi et al. [78].

In this context, the present study adopts an integrated experimental framework combining destructive and non-destructive testing in order to better understand the evolution of the

mechanical properties and tensile behavior of mortar with predefined geometric heterogeneities (cracks and voids). The evolution of Young's modulus and Poisson's ratio was first monitored by ultrasound at 7, 14, and 28 days, allowing repeated measurements on the same specimens and reducing variability due to sample differences. In parallel, a calibration was performed using three-point bending tests to establish a link between dynamic and static properties, leading to a linear empirical equation of the type $E_s = a \times E_d + b$ adapted to the studied mortar. Quasi-static direct tensile tests were then used to analyze the structural response and crack propagation. The experimental characterization results show a gradual but non-regular increase in stiffness as the specimen ages, reflecting a continuous densification of the microstructure. The tensile tests confirm this evolution, with a slight increase in the critical load between 7 and 14 days, followed by a much more marked increase between 14 and 28 days. The experimental originality of this work lies in combining the monitoring of changes in mechanical properties with the age of mortar and the tensile response of mortars on test specimens with predefined geometric heterogeneities (cracks and voids), thus giving a more representative and integrated view of the tensile behavior of cementitious mortars at different ages.

Numerically, this study adopts a specific implementation of the phase field approach to modeling the crack propagation in the mortar under study. The variational formulation has been decomposed into two coupled equations, one for displacement and the other for damage, solved by an explicit alternating minimization strategy implemented in a MATLAB® code developed for this work. This methodology ensures enhanced numerical stability and reproducibility of the protocol, consistent with the experimentally measured mechanical parameters (E, θ, G_c). The choice of the regularization parameter ℓ was physically justified by the sand grain size, establishing a direct correspondence between the microstructural scale and the numerical model. Finally, an original double-domain strategy was introduced: in the logical domain, the complete experimental configuration is reproduced, while in the physical domain, the mechanical effect of the tubes is replaced by a simplified condition ($\Phi = 0$) at the edges. This dual modeling approach allows for cross-validation and highlights the consistency between numerical and experimental results. The numerical originality of this work thus lies in the adaptation of the phase field to the experimental conditions studied, paving the way for a better understanding of cracking in cementitious mortars.

This article is structured as follows: Section 2 presents the experimental procedure and protocol adopted, including a granulometric analysis of the sand used, as well as a detailed description of the mixture prepared and the specimens produced. A characterization of the material parameters, notably the modulus of elasticity E_s and the fracture energy of the material G_c , is then carried out using a non-destructive characterization (NDT) technique via an ultrasonic device. The direct tensile test adopted is then described in detail. Section 3 summarizes the experimental results obtained during the direct tensile tests, together with a comparative and explanatory analysis. In Section 4, the theoretical aspects and numerical implementation of the phase-field approach adopted are presented. Section 5 presents the numerical results, with comments and comparisons with experimental observations. Finally, the most pertinent conclusions are drawn in Section 6, bringing this paper to a close.

2. Experimental procedure and protocol

2.1. *Granulometric analysis of sand*

The test involves classifying the various grains in the specimen using a series of sieves, arranged in a stack with progressively smaller mesh sizes from top to bottom.

The sand specimen is placed in the top sieve, and the grain classification is obtained by vibrating the sieve stack.

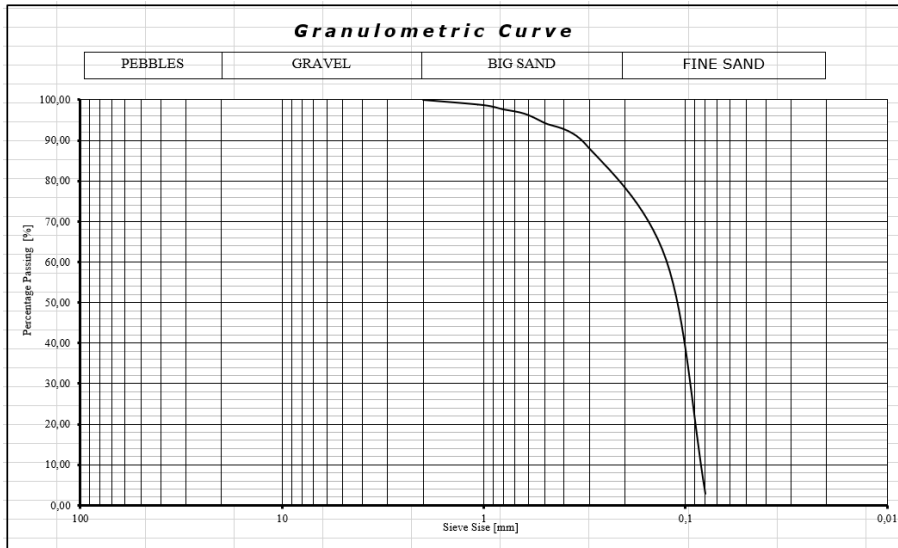


Figure 1. The granulometric curve of the sand.

Table 1. Mixture proportions use

Component	Cement	Sand	Water
Percentage	22%	66%	12%
Dosage	459.53 Kg/m ³	1378.59 Kg/m ³	250.65 Kg/m ³

For this test, we use a series of sieves with square mesh by their aperture classified as follows: 0.08–0.125–0.315–0.5–0.63–0.8–1–2 (mm).

The granulometric curve of sand is shown in Figure 1 according to the standard NF P18-431 [Afn, P 18-431-1990].

The granulometric curve shows that our sand has a well-distributed particle size range, with the majority of particles falling between 0.1 mm and 1 mm, classifying it as medium sand. The grading curve is relatively smooth, indicating a uniform particle size distribution and confirming that the sand is well-graded.

2.2. Preparation of the mixture

The material used was a standard mortar with the following proportions: 22% cement (Portland cement PC40 mixed with high alumina cement in a 4:1 ratio, conforming to ASTM C595), 66% sand (particle size < 1 mm), and 12% water (clean, impurity-free water), resulting in a water/cement ratio of 0.55.

The dosages of the constituents used in this study are presented in Table 1. These standard specifications were selected to minimize uncertainties in the mix by excluding other influencing factors, such as additives.

By adopting a standardized mortar formulation, composed of well-graded sand (particle size range between 0.1 and 1 mm) and free from admixtures, we deliberately minimized external sources of variability in the mechanical behavior of the material. This methodological choice ensures that the fracture response observed during the direct tensile tests (see Section 3) is mainly governed by the predefined discontinuities introduced in the specimens and by the influence of specimen age, which represent the central focus of the present study.

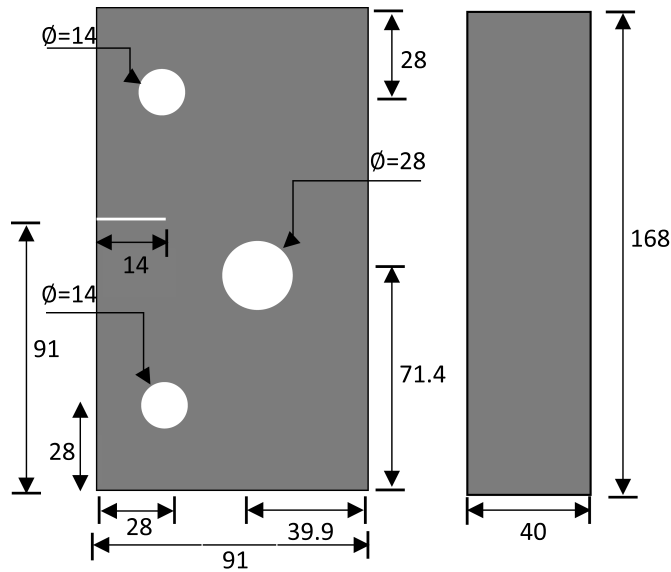


Figure 2. Geometry of the test specimen used in this study.

2.3. Preparation of the test specimen

The test specimen used in this study is a rectangular parallelepiped with dimensions of $W = 91$ mm (width), $H = 168$ mm (height), and $e = 40$ mm (thickness). The specimen features several geometric characteristics: a circular cutout with a diameter of 28 mm located near the center of the plate ($x = 51.1$ mm, $y = 71.4$ mm), and two smaller cutouts with a diameter of 14 mm near the top and bottom, positioned at ($x = 28$ mm, $y = 28$ mm) and ($x = 28$ mm, $y = 140$ mm), respectively. Additionally, the plate has an initial crack of length $a_0 = 14$ mm on its left side, located at $y = 91$ mm (see Figure 2).

The steps for preparing the test specimen are detailed in Appendix A.

2.4. Material characterization of the test specimen

2.4.1. Estimation of Young's modulus and Poisson's ratio using non-destructive tests (ultrasound)

The estimation of mechanical properties through destructive testing provides reliable results but requires the use of different specimens for each measurement age. Even when mix proportions and curing conditions are identical, slight variations related to particle size distribution or microstructure may arise from one specimen to another, introducing variability that can obscure the actual effect of age. To overcome this limitation, the ultrasonic method was adopted. Its major advantage lies in allowing repeated measurements on the same specimen without altering it, thereby providing a more representative and accurate monitoring of the evolution of Young's modulus and Poisson's ratio as a function of age, while reducing experimental dispersion between test series. In this study, this non-destructive ultrasonic approach was implemented to characterize mortar at different curing stages, namely at 7, 14, and 28 days. The targeted elastic properties, namely the dynamic Young's modulus E_d and Poisson's ratio ν , were determined using this method. The selected propagation mode was direct transmission, as illustrated in Figure 3.

The ultrasonic technique enables the measurement of the propagation times of longitudinal pulses (t_p , P -waves) and shear pulses (t_s , S -waves) through the mortar. These propagation times

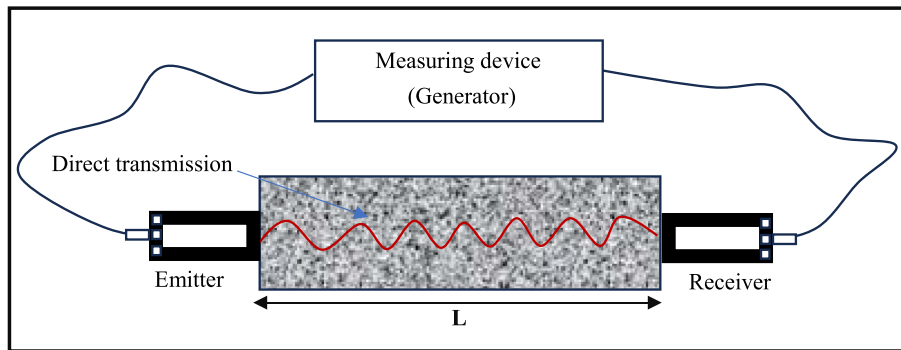


Figure 3. The ultrasonic testing principle.

are then used to calculate the corresponding wave velocities, V_p and V_s , which are required for the determination of the dynamic Young's modulus E_d and Poisson's ratio ϑ , using the equations presented in (2) and (3) [36,37].

The ultrasonic device consists of a generator connected to a transmitter and a receiver of electrical pulses, as illustrated in Figure 3. Piezoelectric crystals excited by impact generate the pulses, while similar crystals in the receiver detect them. The receiver, coupled with a timing unit, records the propagation time between the emission and detection of the pulse. Based on these measurements, the propagation velocities of longitudinal waves V_p and shear waves V_s are obtained as follows [36,37]:

$$V_p = \frac{L}{(2 \times t_p)}, \quad V_s = \frac{L}{(2 \times t_s)} \quad (1)$$

where L is the distance between the transducers, t_p and t_s are the propagation times of the longitudinal and shear pulses, respectively. These velocities are then used to determine the dynamic Young's modulus E_d and Poisson's ratio ϑ of the mortar, according to the following relations [36,37]:

$$E_d = V_p^2 \gamma \frac{(1 + \vartheta)(1 - 2\vartheta)}{(1 - \vartheta)} \quad (2)$$

$$\vartheta = \frac{V_p^2 - 2V_s^2}{2(V_p^2 - V_s^2)} \quad (3)$$

where γ is the density of the specimen (kg/m^3), V_p is the longitudinal wave velocity (m/s), V_s is the shear wave velocity (m/s), E_d is the dynamic Young's modulus (GPa), and ϑ is Poisson's ratio.

Equations (2) and (3) are valid under the assumption that the material behaves as an elastic, homogeneous, and isotropic medium at the macroscopic scale, and that ultrasonic waves propagate in the linear regime without significant attenuation. Although cementitious materials exhibit a complex microstructure, these relations have been widely employed and validated in numerous studies on pastes, mortars, and concretes for the evaluation of their mechanical properties [35–37,39,79]. The use of a standard mortar (sand, cement, water), as described in Section 2.2, also helps to minimize the influence of heterogeneities associated with coarse aggregates and to ensure a globally homogeneous and isotropic behavior at the considered scale. In this context, the application of Equations (2) and (3) is justified and consistent with commonly accepted practices in the literature.

Table 2 summarizes the average values obtained from non-destructive tests performed on nine specimens at 7, 14, and 28 days of curing. For detailed results corresponding to each specimen, the reader is referred to Tables A1–A3 in Appendix A.

Table 2. Results of non-destructive tests

	Longitudinal wave V_p (m/s)	Shear wave V_s (m/s)	Poisson's ratio average ϑ	Dynamic Young's modulus average E_d (GPa)
7 days	4.8942×10^3	2.9773×10^3	0.2062	44.6653
14 days	5.3061×10^3	3.2233×10^3	0.2076	52.4081
28 days	6.2760×10^3	3.8022×10^3	0.2100	73.0781

Table 2 highlights a progressive and significant increase in the dynamic Young's modulus E_d with mortar age, while the Poisson's ratio ϑ remains relatively stable. This evolution is directly related to the ultrasonic velocities V_p and V_s , used in Equations (2) and (3). Indeed, the gain in material stiffness is reflected by an increase in propagation velocities, particularly the longitudinal wave velocity V_p , which mechanically induces an elevation of E_d .

At 7 days, the dynamic Young's modulus E_d reaches approximately 45 GPa, indicating a still limited stiffness of the material, which can be explained by the relatively low measured wave velocities V_p and V_s (see Tables A1–A3 in Appendix A). Between 7 and 14 days, the increase in E_d remains moderate ($\approx +15\%$), corresponding to a slight variation in ultrasonic velocities and reflecting a gradual consolidation of the microstructure with a limited gain in compactness. In contrast, between 14 and 28 days, the increase in E_d is much more pronounced ($\approx +35\text{--}40\%$) and is accompanied by a significant rise in both V_p and V_s (see Tables A1–A3 in Appendix A). This evolution indicates a substantial reduction in porosity and improved matrix continuity, directly enhancing load transfer and thus the elastic properties.

Furthermore, the Poisson's ratio, determined according to Equation (3), remains nearly constant throughout the entire period studied, indicating that the increase in Young's modulus is mainly driven by the joint growth of V_p and V_s , without significant variation in their ratio. For detailed information on the individual values of V_p , V_s , E_d , and ϑ for each specimen, the reader is referred to Tables A1–A3 in Appendix A.

Particular attention has been given to the comparison between static Young's modulus E_s and dynamic Young's modulus E_d for different types of rocks, with numerous empirical formulas reported in the literature [34,38]. These formulas are either linear, as shown in Equation (4), or nonlinear, as shown in Equation (5).

$$E_s = a \times E_d + b \quad (4)$$

$$E_s = a \times (E_d)^b. \quad (5)$$

The nonlinear relationship Equation (5) is generally considered more representative for materials and rocks exhibiting significant microcracking or relatively high porosity, cases in which E_s increases more slowly than E_d ($b < 1$). In contrast, the linear form Equation (4) remains applicable to more compact and homogeneous materials. In the present study, and for a standard mortar as described in Section 2.2, the linear form Equation (4) was adopted, as it is widely used in the literature for both rocks and cementitious materials [80–83]. In all cases, the empirical coefficients a and b must be experimentally determined for each mortar formulation to ensure the reliability and relevance of the correlation.

The application of Equation (4) requires the definition of the empirical parameters a and b , which are strongly dependent on the type of material investigated. To establish a representative relation for the mortar under consideration, a specific experimental calibration was undertaken. For this purpose, the static Young's modulus E_s was determined from three-point bending tests performed on nine prismatic specimens with dimensions of $160 \times 40 \times 40 \text{ mm}^3$ at the age of 14 days, in accordance with the Russian State Standard GOST 310.4-81 [32,33]. The test was conducted under a monotonically applied load of 2.5 kN, as illustrated in Figure 4.

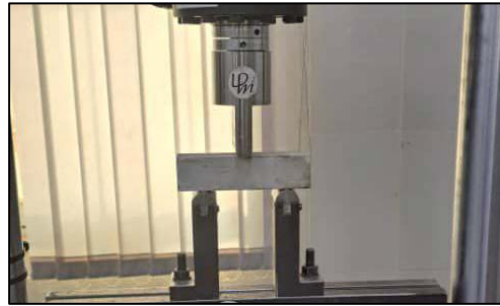
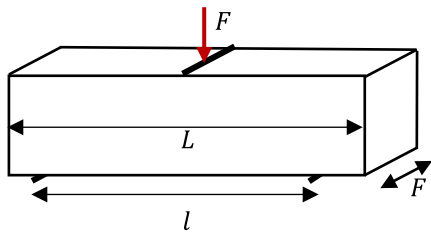


Figure 4. Experimental setup of the three-point bending test performed on prismatic specimens with dimensions of $160 \times 40 \times 40 \text{ mm}^3$ at the age of 14 days.

Table 3. Experimental results of the three-point bending test at 14 days: average values of the applied load, the corresponding deflection, and the static Young's modulus $E_s^{(14)}$

The load F (kN)	The deflection δ (mm)	The slope $\Delta F / \Delta \delta$ (KN/mm)	The static Young's modulus $E_s^{(14)}$
0.229	0.03878		
0.458	0.07756		
0.687	0.11634		
0.916	0.15512		
1.145	0.19390	5.905105724600306	0.5764891
1.374	0.23268		
1.603	0.27146		
1.832	0.31024		
2.060	0.34902		

The choice of 14 days for this calibration is justified by its representativeness in the microstructural evolution of the mortar. Indeed, this intermediate age makes it possible, on the one hand, to reduce the influence of the high mechanical variability generally observed at early ages (7 days), and on the other hand, to avoid the quasi-complete stabilization effects of mechanical properties typically observed at 28 days.

The static Young's modulus was then calculated from the mean force–deflection curves, using the classical relation [32,33]:

$$E_s = \frac{l^3}{4bh^3} \frac{\Delta F}{\Delta \delta} \quad (6)$$

where l is the span between supports (100 mm), b and h are the dimensions of the cross-section (40 mm \times 40 mm), F is the applied load (kN), and δ is the measured deflection (mm).

The average load and deflection results from nine specimens, taken at selected points within the linear elastic range, are presented in Table 3.

In parallel, the dynamic Young's modulus E_d was measured on the same specimens using the ultrasonic method, which provided a representative average value at this age. The combined introduction of E_s and E_d values into the linear empirical equation (Equation (4)) then allowed the determination of the parameters a and b . Considering the physical condition that $E_s = 0$ when $E_d = 0$, it was deemed appropriate to set $b = 0$, thereby simplifying the relation to a direct proportionality between the two moduli: $E_s = a \times E_d$.

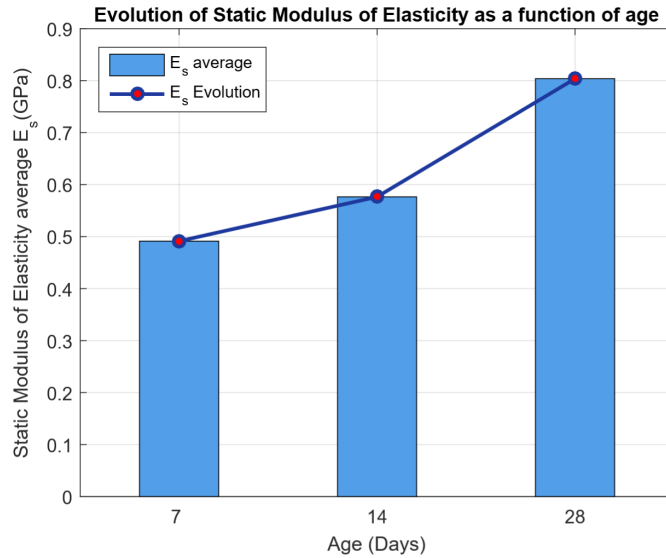


Figure 5. Evolution of the average static Young's modulus with curing age (7, 14, and 28 days).

The proportionality coefficient a was experimentally determined to be 0.011 for the mortar under investigation. Accordingly, the specific relation obtained is:

$$E_s = 0.011 \times E_d. \quad (7)$$

This calibrated empirical equation was subsequently employed to estimate the static Young's modulus E_s at other ages (7 and 28 days) from the available dynamic measurements. It thus provides a reliable tool to non-destructively monitor the evolution of the mortar's elastic modulus as a function of age.

Figure 5 illustrates the evolution of the average static Young's modulus E_s with curing age. For detailed E_s values corresponding to each specimen, calculated from Equation (7), the reader is referred to Tables A1–A3 in Appendix A.

The evolution of Young's modulus with age, illustrated in Figure 5, highlights the progressive increase in material stiffness during curing. The static modulus E_s exhibits a trend similar to E_d , since it is linearly proportional to it. More specifically, the value of Young's modulus increases from approximately 0.49 GPa at 7 days to 0.58 GPa at 14 days. Between 14 and 28 days, this increase becomes more pronounced, reaching 0.80 GPa at 28 days. This evolution reflects the progressive densification of the microstructure, with improved compactness and matrix continuity, which directly enhances material stiffness. The histogram, complemented by the trend curve, clearly illustrates this behavior and emphasizes that the development of mechanical properties is not linear but intensifies after two weeks of curing.

2.4.2. Estimation of fracture energy

The fracture Energy G_c (N/mm) is a crucial parameter in the phase field model. For normal concrete mortar, G_c (N/mm) is determined from the fracture resistance W_F as follows (see in [84–87]):

$$G_c = \frac{W_F + M \times g \times u_0}{A}. \quad (8)$$

In this equation, we define M as the weight of the specimen (kg); g as the acceleration due to gravity $9.81 \text{ (m/s}^2\text{)}$; u_0 as the critical imposed displacement (m); A as the cross-sectional area at the initial crack (m^2). The fracture resistance W_F represents the area under the load–displacement curve at the maximum value of u_0 .

The expression adopted for the estimation of the fracture energy G_c (Equation (8)) is derived from the work-of-fracture method in the framework of quasi-static tensile tests (direct tension, three-point bending, or splitting test). Its validity relies on several assumptions that must be specified. First, the loading must be monotonic and sufficiently slow so that dynamic and rate effects are negligible. Second, crack propagation is assumed to occur in pure mode I (opening), without significant contribution from shear or mixed-mode effects. The material is considered homogeneous, well-compacted, and isotropic at the macroscopic scale, with a well-defined notch or initial crack to ensure reproducible initiation. Finally, this formulation is restricted to monotonic loading up to crack propagation and does not account for cyclic, viscoelastic, or size effects. Under these conditions, the equation provides a consistent estimation of the fracture energy of cement-based materials, as demonstrated in the seminal works of Hillerborg et al. and RILEM TC 50-FMC [86,87].

For the mortar investigated in this study, the fracture energy calculated using Equation (8) is given by:

$$G_c = \frac{0.2 + 1.2 \times 9.81 \times 0.25 \times 10^{-6}}{40 \times 70 \times 10^{-6}} = 72.48 \text{ (N/m)}. \quad (9)$$

2.5. *The principle of the test adopted*

Direct tensile tests were performed using an MTS hydraulic testing machine (capacity 100 kN), as illustrated in Figure 6. The specimens were fixed by means of rods inserted into dedicated holes, ensuring symmetric alignment between the upper and lower grips. Prior to each test, a slight preload was applied to eliminate any residual play and to guarantee the absence of initial stresses. The tensile test was then conducted under displacement control: a total displacement of 1.5 mm was progressively applied over a duration of 3000 s (loading velocity 0.0005 mm/s), thereby ensuring quasi-static conditions suitable for accurately capturing the brittle behavior of the specimens up to failure. The testing machine was equipped with a load cell with a precision of $\pm 0.5\%$ and a displacement transducer with a resolution of 0.001 mm, ensuring sufficient sensitivity to detect fine variations in load and displacement.

3. Experimental results

In this section, the experimental results obtained during the test adopted in Figure 6 are presented as follows.

Tables 4, 5, and 6 present the experimental results of the tensile tests conducted at 7, 14, and 28 days, respectively. The load–displacement curves show that specimens of the same age exhibit a consistent evolution, with only slight variations in the critical load and displacement values, as detailed in Tables 4–6. Analysis of these results indicates that the differences observed, although modest, exceed the limit of instrumental sensitivity and are likely related to the intrinsic heterogeneity of the mortar (component distribution, initial microcracks, local porosity), as well as slight variations in specimen positioning or alignment. Nevertheless, the overall consistency of the values obtained confirms the good reproducibility of the experimental method.

The structure behaves linearly up to the maximum loading. After that, a brutal drop can be identified when the crack begins to propagate.

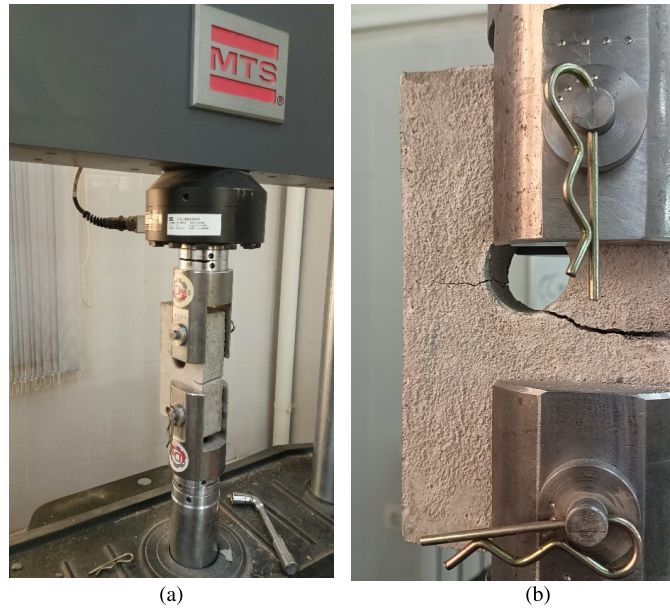


Figure 6. (a) The direct tensile test; (b) crack propagation in specimen.

Table 4. Experimental results obtained at 07 days of age (a) damage evolution in specimen 01; (b) damage evolution in specimen 02; (c) load–displacement curves

<p>(a)</p>	<p>(b)</p>	<p>(c)</p>
<p>— Specimen(01)</p> <p>— Specimen(02)</p>	<p>$F_1 = 1.028 \text{ [KN]}$</p> <p>$F_2 = 0.9899 \text{ [KN]}$</p>	<p>$U_{c1} = 0.2377 \text{ [mm]}$</p> <p>$U_{c2} = 0.2213 \text{ [mm]}$</p>

Figure 7 compares the effort–displacement curve as a function of age factor. The evolution of the maximum load F_{max} as a function of age exhibits two distinct phases. Between 7 and 14 days, the increase remains limited (+12%), reflecting a progressive but still incomplete consolidation of the microstructure. In contrast, between 14 and 28 days, the progression becomes much more pronounced (+45%), indicating a significant reduction in porosity and an improved continuity of the matrix, which directly enhances stress transmission.

This trend is consistent with the results obtained for the Young’s moduli (Section 2.4). In particular, the dynamic modulus E_d shows a moderate increase between 7 and 14 days ($\approx +15\%$),

Table 5. Experimental results obtained at 14 days of age (a) damage evolution in specimen 03; (b) damage evolution in specimen 04; (c) load–displacement curves

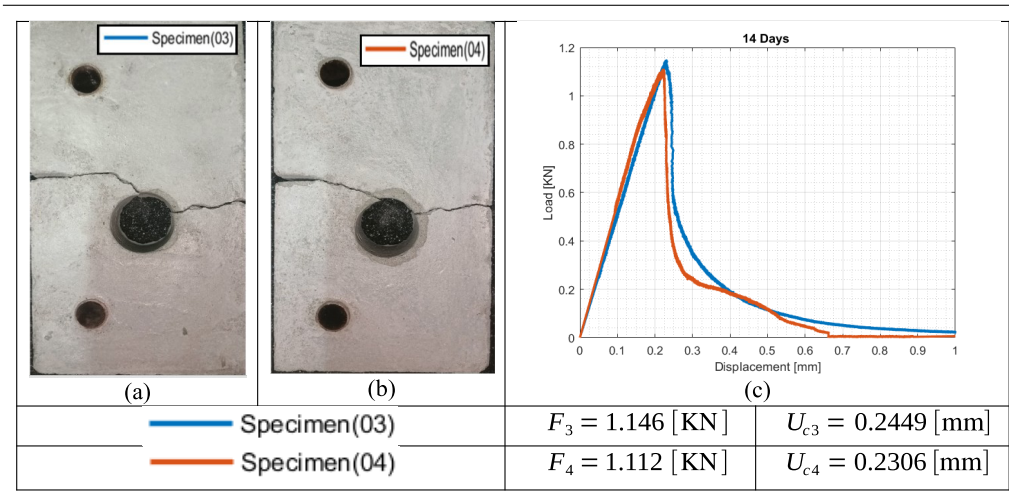
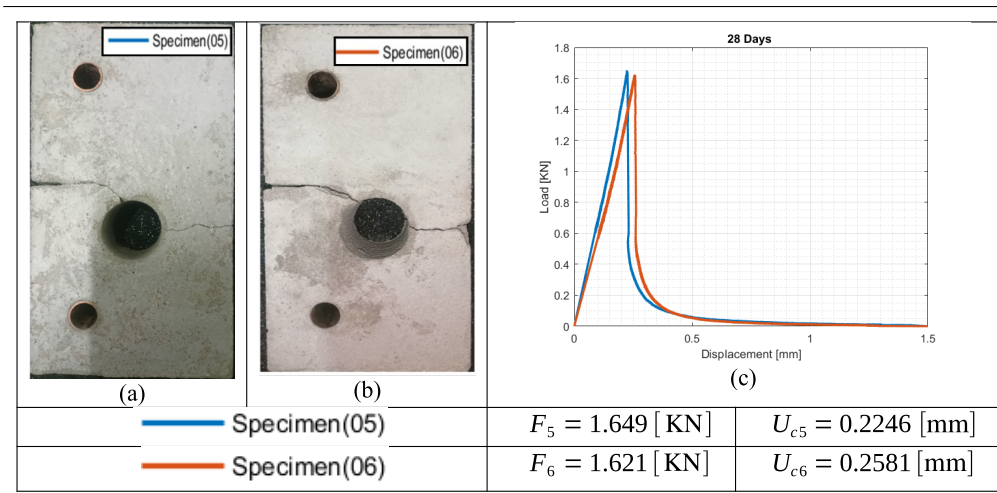


Table 6. Experimental results obtained at 28 days of age (a) damage evolution in specimen 05; (b) damage evolution in specimen 06; (c) load–displacement curves



followed by a marked acceleration between 14 and 28 days ($\approx +35\text{--}40\%$), in line with the increase in ultrasonic velocities. The static modulus E_s evolves in the same manner. Thus, the correlation between mechanical strength, static modulus, and dynamic modulus confirms that the significant increase observed between 14 and 28 days does not result from an experimental artifact, but rather reflects a genuine microstructural transformation.

4. Phase field modeling

The phase-field model has proved to be a reliable and practical approach for predicting crack initiation and propagation. In this section, we present the main equations of the phase-field

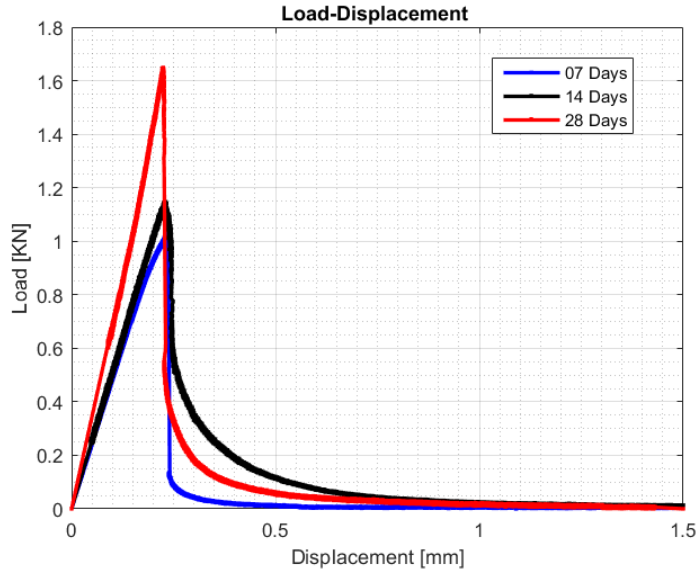


Figure 7. Comparison of the load–displacement curves at ages 7, 14, and 28 days.

approach to brittle fracture, as well as its implementation by the finite element method under our calculation code developed on MATLAB®. The modeling strategy followed to reproduce the experimental tensile tests is also detailed and validated.

4.1. Theoretical aspects

In the present study, we have chosen to adopt and use the theoretical framework defined by Francfort and Marigo [47,88,89], with the aim of addressing and overcoming the shortcomings of Griffith’s 1998 theory [4]. They express the phenomenon fracture for a linear elastic domain Ω that may contain a set of cracks Γ as a competition between the surface energy required for crack propagation Π_s and the elastic energy Π_e stored in the material in the form of a variational theory as a function of the displacement field u .

The total potential energy of the Ω domain can be written as:

$$\Pi_p(u, \Gamma) = \Pi_e(u, \Gamma) + \Pi_s(u, \Gamma) - \mathcal{W}^{\text{ext}}(u) \tag{10}$$

$$\Pi_e(u, \Gamma) = \int_{\Omega} W_0(\varepsilon(u), \Gamma) \, d\Omega \tag{11}$$

$$\Pi_s(\Gamma) = \int_{\Gamma} G_c H^{n-1}(\Gamma) \, d\Gamma \tag{12}$$

$$\mathcal{W}^{\text{ext}}(u) = \int_{\Omega} f \cdot u \, d\Omega + \int_{\partial\Omega_u} t \cdot u \, d\Gamma \tag{13}$$

$$\Pi_p(u, \Gamma) = \int_{\Omega} W_0(\varepsilon(u), \Gamma) \, d\Omega - \int_{\Omega} f \cdot u \, d\Omega - \int_{\partial\Omega_u} t \cdot u \, d\Gamma + \int_{\Gamma} G_c H^{n-1}(\Gamma) \, d\Gamma \tag{14}$$

where $\varepsilon(u) = 1/2[\nabla \otimes u + u \otimes \nabla]$ is the symmetrical tensor of small strains, $t = \sigma \cdot n$, σ and n being respectively the stress tensor and the exterior normal to the boundary $\partial\Omega_u$, H^{n-1} is the $(n-1)$ dimensional Hausdorff measure giving the surface associated with Γ , $W_0(\varepsilon(u))$ is the elastic energy density.

In the present work, the formulation is restricted to the case of displacement-controlled loading (Dirichlet conditions). In this configuration, the external work term $\mathcal{W}^{\text{ext}}(u)$ vanishes,

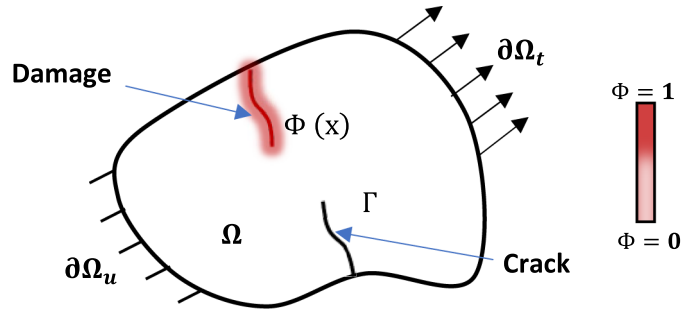


Figure 8. A solid body Ω with a conventional sharp crack Γ and diffuse crack band in phase-field $\Phi(x)$.

since at each loading step the displacement gradient is zero. Conversely, when force-controlled loading (Neumann conditions) is considered, this term must be explicitly accounted for, which may induce a loss of convexity of the functional and lead to numerical convergence difficulties toward a global minimum in the alternate minimization scheme, as noted by Amor [90]. This restriction therefore corresponds to an implementation choice motivated both by numerical stability considerations and by the aim of faithfully reproducing the experimental conditions described in Section 2.5, which were conducted under displacement-controlled loading.

The total energy function is expressed by:

$$\Pi_p(u, \Gamma) = \int_{\Omega} W_0(\varepsilon(u), \Gamma) d\Omega + \int_{\Gamma} G_c H^{n-1}(\Gamma) d\Gamma. \quad (15)$$

Considering all possible cracking states, the evolution of the crack set Γ as well as the unknown displacements u is determined by the global minimization of functional (15), under the irreversibility constraint, as follows:

$$\Pi_p(u_i, \Gamma_i) = \min_{\Gamma_{t+\Delta t} \supseteq \Gamma_t} \Pi_p(u, \Gamma). \quad (16)$$

In the case of brittle fracture, the fracture energy G_c can be interpreted as Griffith's critical energy restitution rate. The challenge of solving the surface integral directly arises from the fact that the new $\Gamma(t)$ surfaces are unfamiliar at first sight. Conversely, classical discretization methods fail to produce a satisfactory resolution.

The main difficulty in minimizing the previous variational formulation, given by functional (15), lies in the need to anticipate all possible cracking states. In other words, it is necessary to construct discontinuous displacement fields on arbitrary discontinuity surfaces, which is beyond the capabilities of conventional finite element methods. To make the problem tractable, Bourdin et al. [48] adopted an alternative approach, where minimization is performed on a regularized approximation of the Griffith functional. This regularization introduces smoothed displacement discontinuities, ensuring the continuity of the displacement field u across the entire domain. This approach is inspired by the work of Ambrosio and Tortorelli [91], who solved a similar problem in the context of image segmentation, in connection with the function of Mumford and Shah [92].

From the mechanical point of view, this regularization approach makes it possible to reformulate fracture models using a phase field model, thus introducing a parameter $\phi(x, t) \in [0, 1]$. It is based on replacing the sharp discontinuity in the displacement field, representing the crack, with a gradual transition within small zones where the displacement gradient is high (damaged zones). The size of these zones is regulated by a parameter ℓ , while their characteristics are determined by the damage variable $\phi(x, t) \in [0, 1]$, as illustrated in Figure 8.

Since the crack is represented as a damaged zone, an exponential decay function is used to approximate its irregular topology. In one dimension, in order to represent a crack located at $x = 0$, a specific formulation of the second-order phase field is adopted [48,72]:

$$\Phi(x) = \exp\left(\frac{-|x|}{2\ell}\right). \tag{17}$$

In Equation (17), $\phi(x, t) \in [0, 1]$, with 0 representing undamaged material and 1 indicating complete material damage. This equation represents the solution of a homogeneous ordinary differential equation [55,72,93]:

$$\Phi''(x) - \frac{1}{2\ell}\phi(x) = 0 \quad \text{in } \Omega. \tag{18}$$

The differential equation (18) is solved under Dirichlet-type boundary conditions:

$$\begin{cases} \Phi(0) = 1, & \phi'(0) = 0 \\ \lim_{x \rightarrow +\infty} \phi(x) = \lim_{x \rightarrow -\infty} \phi(x) = 0 & \text{and,} \\ \lim_{x \rightarrow +\infty} \phi'(x) = \lim_{x \rightarrow -\infty} \phi'(x) = 0. \end{cases} \tag{19}$$

The Equation (18) represents the strong formulation corresponding to the variational problem:

$$\Phi(x) = \text{Arg}(\inf I(\phi)) \tag{20}$$

were

$$I(\phi) = \frac{1}{2} \int_{\Omega} (\phi^2 + (2\ell)^2 G_c \nabla \phi^2) \, d\Omega \quad \text{were } d\Omega = \Gamma_{\ell} \, dx.$$

Therefore, we introduce $\Gamma_{\ell}(\phi)$ to describe the second-order phase-field approach, defined as follows:

$$\Gamma_{\ell}(\phi) = \frac{1}{2\ell} I(\phi) = \frac{1}{4\ell} \int_{\Omega} (\phi^2 + (2\ell)^2 \nabla \phi^2) \, d\Omega. \tag{21}$$

The choice of the coefficients of $\phi(x)$ and its derivatives in Equation (18) is selected so that:

$$\int_{-\infty}^{+\infty} G_c \Gamma_{\ell}(\phi) \, dx \approx \int_{\Gamma} G_c \Gamma = G_c. \tag{22}$$

Thus, in the context of the second-order phase field, we obtain:

$$\Pi_s(\phi) = \int_{\Gamma} G_c \, d\Gamma = \frac{G_c}{4\ell} \int_{\Omega} (\phi^2 + (2\ell)^2 \nabla \phi^2) \, d\Omega. \tag{23}$$

As proposed by Bourdin et al. [31,32], we approximate the surface energy as follows:

$$\Pi_s(\phi) = \int_{\Omega} G_c \left(\frac{\phi^2}{4\ell} + \ell \nabla \phi^2 \right) \, d\Omega \tag{24}$$

were the choice of the internal length ℓ in this study was guided by the need to ensure good reproducibility of the experimental results. This parameter must remain consistent with the microstructural heterogeneity of the mortar [58,59], while also complying with numerical discretization constraints. In particular, the condition $h_e \ll \ell$ must be satisfied in order to guarantee an accurate resolution of the crack front and the stability of the simulations [60,94].

G_c represents the fracture toughness, defined as the energy required to generate one unit of cracked surface.

As a means of modeling the loss of material stiffness in the fracture zone, i.e. approximating the phase field of the damaged zone, we adopt the approach of Bourdin et al. [48–50], who proposed an isotropic formulation to model the progressive degradation of strain energy and stiffness during crack propagation. Elastic energy is then defined by the following expression:

$$\Pi_e(u, \phi) = \int_{\Omega} [(D(\phi) + \varepsilon_{\ell}) W_0(\varepsilon[u])] \, d\Omega \tag{25}$$

were

$$W_0(\varepsilon[u]) = \frac{1}{2} \sigma : \varepsilon(u) = \frac{1}{2} \varepsilon : \mathbb{C} : \varepsilon = \frac{1}{2} \lambda \, \text{tr}^2 \varepsilon + \mu \, \text{tr}(\varepsilon^2). \tag{26}$$

From the potential of the phase field model, the stress can be calculated by:

$$\sigma(u, \phi) = D(\phi) \frac{\partial W_0(\varepsilon[u])}{\partial \varepsilon[u]} = (1 - \phi)^2 \frac{\partial W_0(\varepsilon[u])}{\partial \varepsilon[u]} \tag{27}$$

$W_0(\varepsilon[u])$ represents the elastic energy density function, while \mathbb{C} is the elasticity tensor, ε and σ designate the strain and stress tensors respectively. The parameters λ and μ are the Lamé coefficients.

The initiation and propagation of cracks are fully described by a problem of minimizing a regularized energy functional. The latter is parameterized by ℓ and expressed according to the following equation:

$$\Pi_t(u, \phi) = \int_{\Omega} \frac{1}{2} (A(\phi) + \varepsilon_{\ell}) \varepsilon[u] : \mathbb{C} : \varepsilon[u] \, d\Omega + \int_{\Omega} \left(\frac{\omega_c(\phi)}{\ell} + G_c \ell \nabla \phi \nabla \phi \right) \, d\Omega \tag{28}$$

where:

$D(\phi) = (1 - \phi)^2$: represents the stiffness degradation function. It is a continuous, strictly decreasing function, which reaches zero only for $\phi = 1$, corresponding to cracking zones.

$\omega_c(\phi) = (\phi^2/4)G_c$ represents the dissipation function. It is a strictly increasing function that takes a zero value when $\phi = 0$.

$A(\phi) = E_0 D(\phi) = E_s (1 - \phi)^2$ represents the elasticity tensor affected by damage.

ε_{ℓ} is a numerical regularization parameter that must be significantly smaller than ℓ .

The phase field model has received various interpretations. Different families of damage models have been proposed, each based on specific choices for the stiffness degradation function $D(\phi)$ and the local dissipation function $\omega_c(\phi)$. For further information, the interested reader may refer to the work mentioned in [48,54,55,72,93].

4.2. The minimization variational framework for the phase field approach

The phase-field model presented above enables us to elucidate crack formation and its spatio-temporal trajectories in the material, without the need for prior specification. This variational framework guarantees its applicability in an elastic medium subjected to displacement-controlled loading, making the quasi-static evolution problem one that seeks to minimize the total energy characterized by the following function:

$$\min \Pi_t(u, \phi) \Rightarrow \Pi_t'^{(u, \phi)} = 0 \tag{29}$$

were

$$(\cdot)'^{(a,b)} = \left(\frac{\partial(\cdot)}{\partial a \partial b} \right).$$

Due to the presence of the term $((1 - \phi)^2 + \varepsilon_{\ell}) w(\varepsilon)$, the functional Π_t is not convex with respect to the pair (u, ϕ) . However, it is observed that, in general, Π_t is convex with respect to each variable separately. In other words, when u is fixed, the functional becomes convex with respect to ϕ , and when ϕ is fixed, it is convex with respect to u . Consequently, by fixing one of the variables, finding the minimum with respect to the other becomes relatively straightforward, as each problem becomes linear after derivation with respect to the corresponding variable. To this end, an alternative has been presented which consists in decomposing the functional (29) into two variational problems which are equivalent to it. Indeed, the:

$$\Pi_t'^{(u, \phi)(\chi, 0)} \left\{ \begin{array}{l} \text{find } u; u \in A_{\delta} \text{ such that, } \forall v \in \mathcal{A}_0 : \\ \int_{\Omega} ((1 - \phi)^2 + \varepsilon_{\ell}) \varepsilon(u) \varepsilon(u) \, d\Omega = 0 \end{array} \right. \tag{30}$$

$$\Pi_t'^{(u, \phi)(0, \Theta)} \left\{ \begin{array}{l} \text{find } \phi; \phi \in H^1(\Omega) \text{ such that, } \forall \Theta \in H^1(\Omega) : \\ \int_{\Omega} \left(-(1 - \phi) \Theta \varepsilon_u[\mathbb{C}] \varepsilon_u + \frac{G_c}{2\ell} \phi \Theta + 2G_c \ell \nabla \phi \nabla \Theta \right) \, d\Omega = 0. \end{array} \right. \tag{31}$$

The test functions χ and Θ are defined to cancel on the boundaries of $d\Omega$, where the Dirichlet conditions are applied.

By solving Equation (30), we obtain the displacement field u that minimizes energy for a fixed ϕ . This solution is then inserted into Equation (31) to determine the damage ϕ that minimizes energy for a fixed u . This process is iterated until the two variables u and ϕ converge.

4.3. Finite element method implementation

In this section, we will attempt to discretize the variational problems set out in Equations (30), (31). We have chosen a triangular element with three nodes located at the vertices and adopted a polynomial interpolation basis of degree 1, where N_s and N_t are respectively the number of nodes and the number of triangles in the mesh.

The development of Equation (30) by applying the finite element method (FEM) discretization gives:

$$\varepsilon_\ell \sum_{e=1}^{N_t} \int_{T_e} [B^u][C][B^\chi] \bar{u}_i \bar{\chi}_j dT_e + \sum_{e=1}^{N_t} \int_{T_e} [B^u][C][B^\chi] \bar{u}_i \bar{\chi}_j dT_e \int_{T_e} (1 - \phi)^2 dT_e = 0. \tag{32}$$

The application of Dirichlet-type boundary conditions on the displacement field cancels out the arbitrary auxiliary test nodal solution $\bar{\chi}_j$, Equation (32) becomes:

$$\varepsilon_\ell \sum_{e=1}^{N_t} \int_{T_e} [B^u][C][B^\chi] \bar{u}_i dT_e + \sum_{e=1}^{N_t} \int_{T_e} [B^u][C][B^\chi] \bar{u}_i dT_e \int_{T_e} (1 - \phi)^2 dT_e = 0. \tag{33}$$

The Equation (33) gives the following linear system:

$$(\varepsilon_\ell [R_{ij}^u] + [R_{i,j}^{u,\phi}]) \{\bar{u}_i\} = 0 \tag{34}$$

were

$$\left\{ \begin{aligned} [R_{ij}^u] &= \sum_{e=1}^{N_t} \int_{T_e} [B^u]^T [C] [B^u] dT_e \\ [R_{i,j}^{u,\phi}] &= \sum_{e=1}^{N_t} \int_{T_e} [B^u]^T [C] [B^u] D(\phi) dT_e \end{aligned} \right. \tag{35}$$

with

$$[D_{r,s}] = \sum_{e=1}^{N_t} \int_{T_e} (1 - \phi)^2 dT_e = \frac{\text{Aire}(T_e)}{6P} \sum_{r,s=i,j,l} (1 - \phi)_r (1 - \phi)_s, \quad \text{such as } P = \begin{cases} 1, & \text{si } r = s \\ 2, & \text{si } r \neq s \end{cases} \tag{36}$$

where i, j, l are the indices corresponding to the node number per element.

$$[D_{r,s}] = \frac{\text{Aire}(T_e)}{6} [(1 - \phi_1)^2 + (1 - \phi_2)^2 + (1 - \phi_3)^2 + (1 - \phi_1)(1 - \phi_2) + (1 - \phi_1)(1 - \phi_3) + (1 - \phi_2)(1 - \phi_3)] \tag{37}$$

were

$$\text{Aire}(T_e) = \frac{1}{2} [(S_y^l - S_y^i)x + (S_x^j - S_x^i)y + (S_x^i - S_x^j) - (S_y^j - S_y^i)].$$

Similarly, the development of Equation (31) gives:

$$\sum_{e=1}^{N_t} \int_{T_e} -(1 - \phi)\Theta\varepsilon[C]\varepsilon dT_e + \sum_{e=1}^{N_t} \int_{T_e} \frac{G_c}{2\ell} \phi\Theta dT_e + \sum_{e=1}^{N_t} \int_{T_e} 2G_c\ell\nabla\phi\nabla\Theta dT_e = 0 \tag{38}$$

$$\sum_{e=1}^{N_t} \int_{T_e} \phi\Theta\varepsilon[C]\varepsilon dT_e + \sum_{e=1}^{N_t} \int_{T_e} \frac{G_c}{2\ell} \phi\Theta dT_e + \sum_{e=1}^{N_t} \int_{T_e} 2G_c\ell\nabla\phi\nabla\Theta dT_e = \int_{T_e} \sum_{e=0}^{N_t} \Theta\varepsilon[C]\varepsilon dT_e \tag{39}$$

$$\begin{aligned} \sum_{e=1}^{N_t} \int_{T_e} [N^\phi][N^\Theta] \bar{\phi}_i \bar{\Theta}_j \varepsilon[C]\varepsilon dT_e + \sum_{e=1}^{N_t} \int_{T_e} \frac{G_c}{2\ell} [N^\phi][N^\Theta] \bar{\phi}_i \bar{\Theta}_j dT_e + \sum_{e=1}^{N_t} \int_{T_e} 2G_c\ell [B^\phi][B^\Theta] \bar{\phi}_i \bar{\Theta}_j dT_e \\ = \sum_{e=1}^{N_t} \int_{T_e} [N^\Theta] \bar{\Theta}_j \varepsilon[C]\varepsilon dT_e. \end{aligned} \tag{40}$$

The application of Dirichlet-type boundary conditions on the damage field cancels out the arbitrary auxiliary test nodal solution Θ_j , Equation (40) becomes:

$$\begin{aligned} \sum_{e=1}^{N_t} \int_{T_e} [N^\phi][N^\Theta] \bar{\phi}_i \varepsilon [C] \varepsilon dT_e + \sum_{e=1}^{N_t} \frac{G_c}{2\ell} [N^\phi][N^\Theta] \bar{\phi}_i dT_e + \sum_{e=1}^{N_t} \int_{T_e} 2G_c \ell [B^\phi][B^\Theta] \bar{\phi}_i dT_e \\ = \sum_{e=1}^{N_t} \int_{T_e} [N^\Theta] \varepsilon [C] \varepsilon dT_e. \end{aligned} \tag{41}$$

The Equation (41) gives the following linear system:

$$(2G_c \ell [R_{ij}^\phi] + [M_{ij}]) \{\bar{\phi}_i\} = \{F_j\} \tag{42}$$

were

$$\begin{cases} [R_{ij}^\phi] = \int_{T_e} [B^\Theta][B^\phi] dT_e \\ [M_{ij}] = \left(\varepsilon [C] \varepsilon + \frac{G_c}{2\ell} \right) \int_{T_e} [N^\phi]^T [N^\phi] dT_e \\ \{F_j\} = \varepsilon [C] \varepsilon \int_{T_k} [N^\Theta] dT_e. \end{cases} \tag{43}$$

The chronological sequence of computational steps associated with all these numerical developments can be summarized by following the framework of the alternating minimization scenario detailed above in the context of the phase field model applied via the finite element method (FEM) according to the following algorithmic structure:

Algorithm 1: Solution algorithm alternate minimization for phase field models

- 1: Set the parameters of this model: ℓ , the internal length of the damage model; ε_ℓ , a rest of rigidity (parameter that ensures the existence and uniqueness of the problem in motion); h , the size of the mesh; δ , the convergence tolerance of the damage model; du discretization of the imposed displacement;
 - 2: **for** the moment: t_I : **do**
 Let $k = 0$ and $\phi^0 := \phi_{t_{i-1}}$ (k is the discretization of the displacement).
 - 3: **As long as** the convergence on d is not achieved **do**
 Conditions at the limits of the Dirichlet type at the moment I applied for the displacement **for** a damage field set in ϕ^k , by using (34) calculate the displacement u^{k+1}
 Conditions at the limits of the Dirichlet type at the moment j applied for the damage **for** a displacement field set in u^{k+1} , by using (42) calculate the damage ϕ^{k+1}
 under reserve of the irreversibility condition $0 \leq \phi_{t_{i-1}} \leq \phi^{k+1} \leq 1$
 $k := k + 1$
end as long as
 $u_{t_i} := u^{k+1}$; $\phi_{t_i} := \phi^{k+1}$
 - 4: **Post-processing calculation:** Evaluation of energies (Π_{ei} , Π_{si}), reactions F_{xi} R_{yi} , ... etc. $i := i + 1$
end for
 $u_i = u_{i-1} + du_i$
-

5. Numerical results

This section is devoted to validating the results obtained with our numerical contribution. To do this, we will proceed in two main stages. Firstly, we will compare our results with analytical solutions using a reference example in simple tension, which will enable us to assess the accuracy and precision of the model employed. At the same time, we will carry out a convergence analysis to ensure the stability and reliability of the calculation code we have developed.

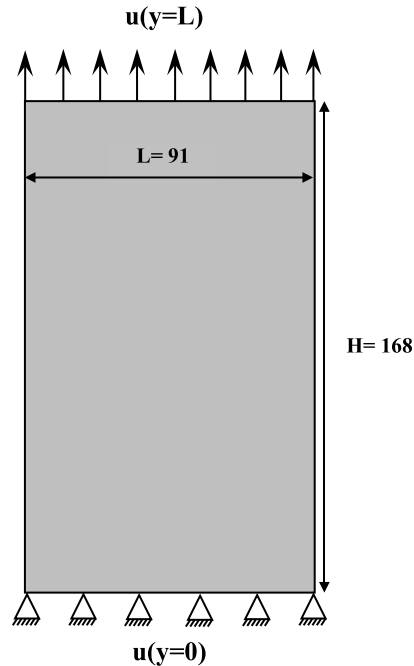


Figure 9. Problem of a rectangular plate under tension loading.

Secondly, we will implement numerical modeling of the experimental tensile tests described in Section 2.5. The aim is to verify experimentally the ability of our calculation code to reproduce the actual behavior of concrete mortar. To this end, we will consider two types of domains: the logical domain, which represents the actual configuration of the problem, and the physical domain, which includes a boundary condition on the damage field aimed at preventing excessive localization of damage at imposed boundaries. A comparative analysis between these two domains will be carried out in order to assess their respective impact on the quality and accuracy of results, and to determine which one proves more appropriate on the basis of experimental results.

5.1. Problem of a rectangular plate under simple tension loading

The case studied concerns a single-axis tensile test applied to a rectangular plate, illustrated in Figure 9, corresponding to the domain $\Omega = (0; L) * (0; H)$ with $L = 91$ mm and $H = 168$ mm. In addition, a zero-displacement condition $u(y = 0) = 0$ is imposed at the lower end, while a displacement-controlled imposed loading is applied at the upper end $u(y = L)$. The other parts of the domain are free. Furthermore, damage is assumed to be zero at the edges where displacement-controlled loading is applied.

The material used is a concrete mortar with the same mechanical parameters found experimentally; Young's modulus $E_s = 0.8$ GPa surface energy density $G_c = 72.48$ N/m, Poisson's ratio $\nu = 0.21$. The numerical regularization parameter is $\varepsilon_\ell = 10^{-5}$ and $\ell = 5 \times 10^{-3}$ m and a loading controlled by imposed displacement $u = N \cdot \check{u} = 4 \times 10^{-4}$ mm with $\check{u} = 4 \times 10^{-7}$ mm and $N = 1000$ imposed displacement steps.

The mesh consists of 32 122 triangular elements and 16 239 nodes, with elements of length $h_e = 0.001$.

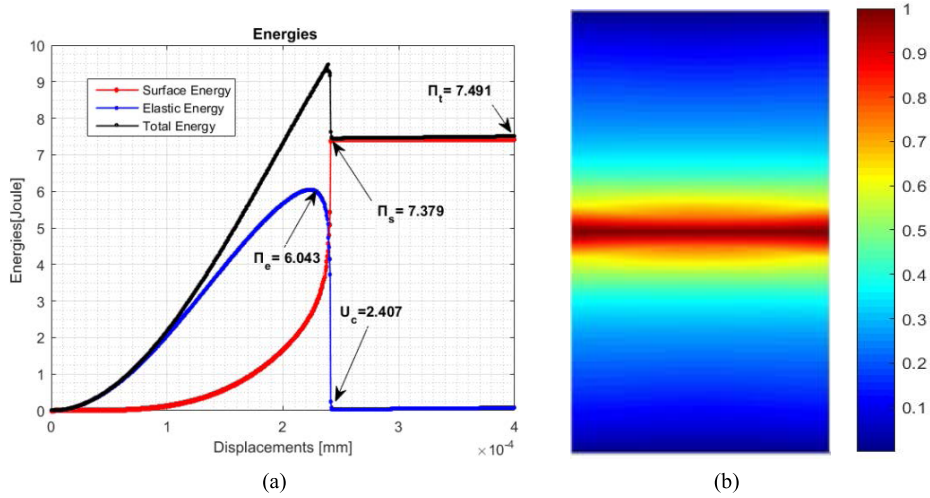


Figure 10. (a) Evolution of energies as a function of imposed displacement; (b) damage distribution.

First, we discuss the analytical results of energy variations, such as the elastic energy, surface energy and total energy, as a function of the loadings u . We then present the critical load that causes damage initiation.

By using the analytical equations [94,95], the energies are presented by:

(1) Elastic energy before rupture:

$$\Pi_e = \int_0^L \frac{1}{2} E_s \frac{\mathbf{u}_c^2}{H^2} dx dy = \frac{1}{2} \frac{E_0 \mathbf{u}_c^2}{H} L = 6.5884 \text{ Joule.} \tag{44}$$

(2) Surface energy:

$$\Pi_s = \int_0^H G_c dx = G_c H = 6.5884 \text{ Joule.} \tag{45}$$

We use energy balance to determine the critical load that causes the structure to fail. This is expressed by the following relationship:

$$u_c^{th} = \sqrt{\frac{2HG_c}{E_0}} 1.743 \times 10^{-4} \text{ mm.} \tag{46}$$

From Figure 10(a), we can see that as long as the loading remains below 1, the structure behaves in a purely elastic manner. However, as soon as this limit is exceeded, a progressive degradation of the material begins, evolving in proportion to the increase in loading. This degradation continues gradually until a critical value of 2.387 is reached, beyond which the damage becomes significant and concentrates in the center of the structure (Figure 10(b)), leading to complete fracture. The evolution of energies confirms this behavior. Elastic energy increases progressively until it reaches a maximum of 0.8979. Once the critical loading value is reached, it decreases sharply until it is cancelled out, and then remains stable at zero. On the other hand, surface energy continues to rise, reaching a maximum of 1.132, where it stabilizes. This represents the total rupture of the structure, confirming the complete separation of the material.

Table 7 compares the analytical solutions with the numerical solutions in terms of the energies-imposed displacement response.

We find that the critical value of the imposed displacement, 2.407×10^{-4} mm, has an estimated error of 38% compared with the analytical value of 1.743×10^{-4} mm. As for surface energy, with a value of 7.379 Joule, the error is 11.99% compared with the analytical value of 6.5884 Joule. This

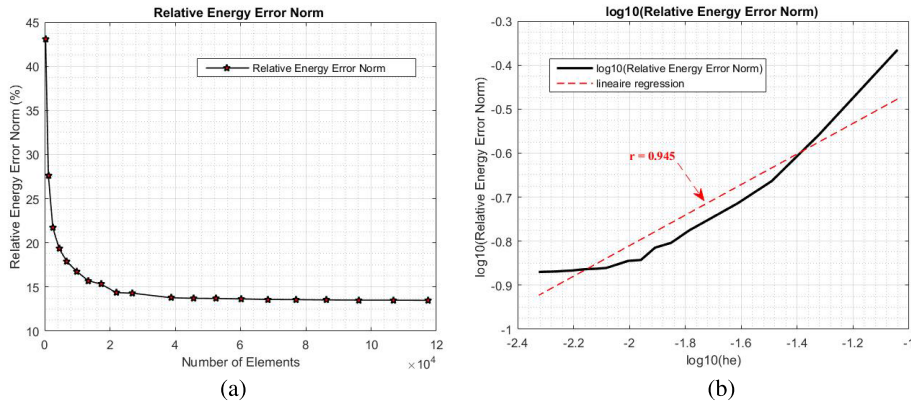


Figure 11. (a) Relative error as a function of number of elements; (b) log(error) as a function of number of elements.

Table 7. Comparison of the numerical results with the analytical results

	Analytical results	Numerical results
Critical displacement u_c (mm)	1.743×10^{-4}	2.407×10^{-4}
Surface energy Π_s (Joule)	6.5884	7.379
Elastic energy Π_e (Joule)	6.5884	6.043
Total energy Π_t (Joule)	6.5884	7.491

latter error is considerably smaller than that observed for critical loading. For the elastic energy, whose value is 6.043 Joule, the error is 8.278% compared with the analytical value of 6.5884 Joule. Finally, for the total energy, whose value is 7.491 Joule, the error is 13.699% compared with the analytical value of 6.5884 Joule.

From the results obtained, we note a relative correspondence between analytical and numerical values, confirming the consistency of the model used.

5.1.1. Convergence study

A convergence analysis is proposed on the basis of the analytical solution, in order to demonstrate the accuracy and stability of the present approach, as well as the efficiency of our developed calculation code. To this end, the relative error in energy norms is evaluated, considering the analytical solution as the exact solution:

$$Er\% = \frac{\|\Pi_t^{he} - \Pi_t^{EX}\|}{\|\Pi_t^{EX}\|}. \tag{47}$$

The numerical solution Π_t^{he} is obtained by running a series of simulations on the current example of a rectangular plate under tension, by varying the mesh size h_e .

The evolution of the error (Er%) as a function of the number of mesh elements is shown in Figure 11(a). It is observed that the error decreases significantly with mesh refinement up to a certain threshold (3.95×10^4 elements), after which it stabilizes, confirming the stability of our developed calculation code.

The rate of convergence is shown in Figure 11(b), where the value of the convergence rate is 0.94 for all configurations, close to 1. This represents near-ideal convergence for a mesh using linear elements, and testifies to the efficiency of our developed calculation code.

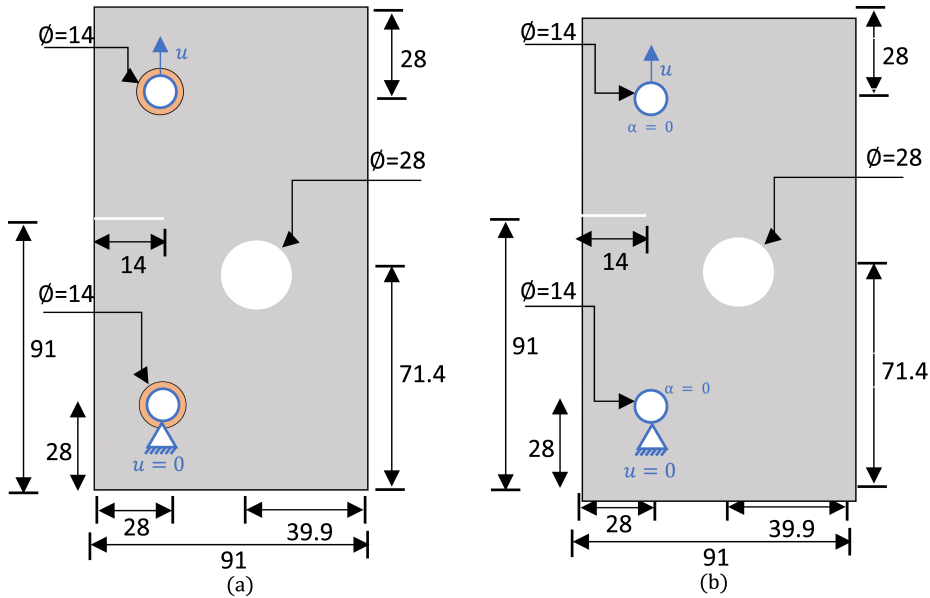


Figure 12. The geometry of the specimen studied (a) logical domain; (b) physical domain.

5.2. Problem of a rectangular plate with a crack and a void

Through our calculation code, we aim to numerically reproduce the tensile test carried out experimentally in (Section 3), using the phase field model implemented by the finite element method (FEM) in (Section 4).

The material used is that experimentally employed in (Section 2), i.e. a concrete mortar with the following mechanical characteristics: Young's modulus $E_s = 0.8$ GPa, Poisson's ratio $\nu = 0.21$, fracture energy $G_c = 72.48$ N/m.

The choice of the internal length $\ell = 0.5 \times 10^{-3}$ m was guided by the granulometric analysis of the sand (Section 2.1, Figure 1), which showed that most grains fall within the 0.1–1 mm range. This value ensures consistency between the mortar's microstructural scale and the regularization parameter of the phase-field model, while guaranteeing both physical representativity and satisfactory numerical stability.

The numerical regularization parameter $\varepsilon_\ell = 10^{-5}$, a loading $u = N \cdot \tilde{u} = 1.5 \times 10^{-3}$ mm with $N = 1000$ step displacement imposed.

To this end, two simulations have been carried out, one on the logical domain and the other on the physical domain. The definition of each domain is described below.

5.2.1. Logical domain

Is the reference domain, the configuration is similar to the experimental test carried out in (Section 2.5, see Figure 6), is a modification of the simple tensile test designed to ensure a homogeneous deformation field in the concrete mortar. The idea is to glue copper tubes to the holes where the displacement-controlled loading is applied. Due to copper's sufficiently high stiffness, this will prevent damage from localizing at the edges of the holes where the loading is applied. The mechanical parameters of the copper used are: Young's modulus $E_{s2} = 128$ GPa, Poisson's ratio $\nu_2 = 0.33$, fracture energy $G_{c2} = 50.096 \times 10^3$ N/m (see Figure 12(a)).

5.2.2. Physical domain

Instead of bonding copper tubes, we apply zero damage ($\phi = 0$) to the edges of the holes where the loading is applied. This condition has the same effect as the previous one, since it avoids localizing damage on these edges (see Figure 12(b)).

To ensure reliable numerical reproducibility of the experimental tests in both configurations investigated (logical domain and physical domain), it is essential to first carry out a mesh convergence study. This step makes it possible to determine the optimal number of elements that guarantees numerical stability, accuracy of the results, and compliance with the regularization conditions imposed by the phase-field model, while minimizing computational cost. To this end, several discretizations of the physical domain were tested by varying the total number of finite elements. The objective is to identify a mesh sufficiently refined to accurately capture crack propagation, while avoiding an unnecessarily high computational cost.

Figure 13 illustrates, on the one hand, the discretized structures corresponding to the different meshes considered, and on the other hand, the evolution of the associated damage field for each mesh, shown in the upper right corner of each illustration. This dual representation enables simultaneous visualization of the influence of mesh refinement on both element distribution and the accuracy of damage modeling.

Figure 14 shows the load–displacement curves obtained for each of the considered meshes. This comparison highlights the influence of mesh density on the simulated mechanical response, particularly in terms of initial stiffness, peak load, and post-peak behavior.

The convergence study highlights the decisive influence of mesh refinement on the accuracy of the numerical results. With coarse meshes, crack trajectories appear diffuse and may deviate slightly from the expected path, while the load–displacement curves reveal an overestimation of the initial stiffness and an inaccurate prediction of the peak load. Moreover, it should be noted that coarse meshes do not satisfy the condition $h_e \ll \ell$. Specifically, for 17 858 elements, the characteristic element size is $h_e = 1.49 \times 10^{-3} \text{ m} > \ell$; for 31 112 elements, it is $h_e = 1.12 \times 10^{-3} \text{ m} > \ell$; and for 47 917 elements, it remains $h_e = 0.9 \times 10^{-3} \text{ m} > \ell$.

From a sufficiently refined mesh (680 025 elements) and beyond, crack propagation becomes stable and well-defined, with no significant variation across different refinement levels. The load–displacement curves then overlap satisfactorily, indicating robust numerical convergence. Accordingly, the adopted mesh (680 025 TRI3 elements) was identified as optimal, ensuring both the reliability and reproducibility of the results.

This choice provides remarkable stability while satisfying the condition $h_e = 0.22 \times 10^{-3} \text{ m} < \ell$.

Figure 15 presents a comparison between the load–displacement curve obtained numerically using the phase-field model with the adopted mesh of 680 025 elements in both the physical and logical domains, and that derived from the experimental results.

The load–displacement response illustrated in Figure 15 shows identical behavior across all curves prior to fracture. The structure first exhibits a linear phase up to the first load drop. Numerically, an elastic rebound corresponding to a load increase (zone A) is then observed, followed by the re-initiation of the crack on the right side of the void and a subsequent abrupt drop. This phenomenon, however, only appears in the numerical results. Experimentally, the load decreases continuously as displacement increases until reaching zero, which corresponds to the complete failure of the specimen.

The divergence observed in zone A can be explained by several mechanisms related to the heterogeneous and relatively low-stiffness nature of mortar. On the one hand, the actual material develops an extended fracture process zone (FPZ) ahead of the crack tip, characterized by microcracking and paste–sand decohesion. Once the crack initiates, the stress field quickly interacts with the large void due to the short distance separating them. A progressive decohesion of

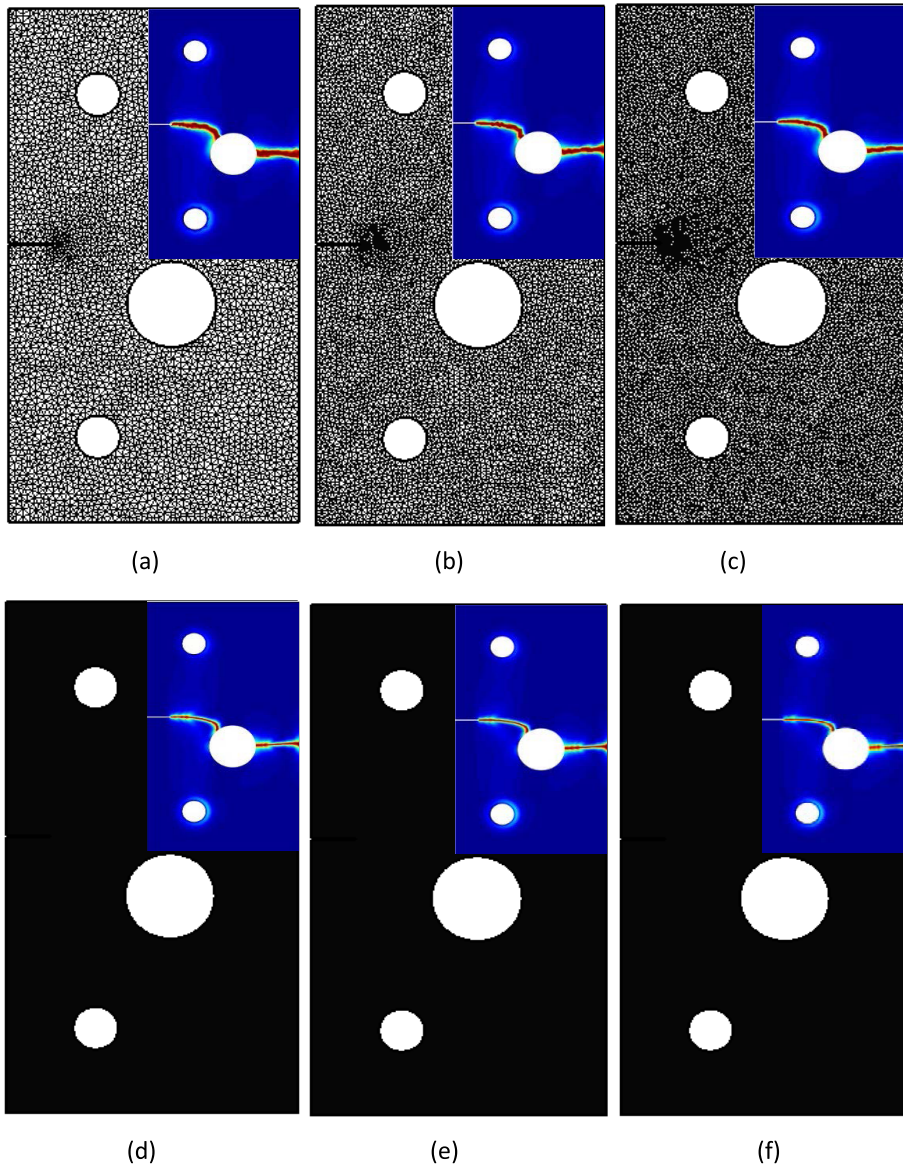


Figure 13. Mesh convergence study: (a) 17 858 elements (TRI3); (b) 31 112 elements (TRI3); (c) 47 917 elements (TRI3); (d) 680 025 elements (TRI3); (e) 728 129 elements (TRI3); (f) 764 438 elements (TRI3).

the interfaces surrounding the void occurs even before the main crack reaches it. Consequently, a significant portion of the mechanical energy is dissipated, such that when the crack eventually reaches the void, it is already “prepared” and can be crossed at a reduced energetic cost. The global response thus manifests as a continuous softening, without the appearance of a distinct second peak.

On the other hand, the numerical model assumes an ideal geometry and treats the mortar as a homogeneous and isotropic material, with dissipation concentrated essentially along the main crack. It does not capture the diffuse decohesion around the void nor the local heterogeneities

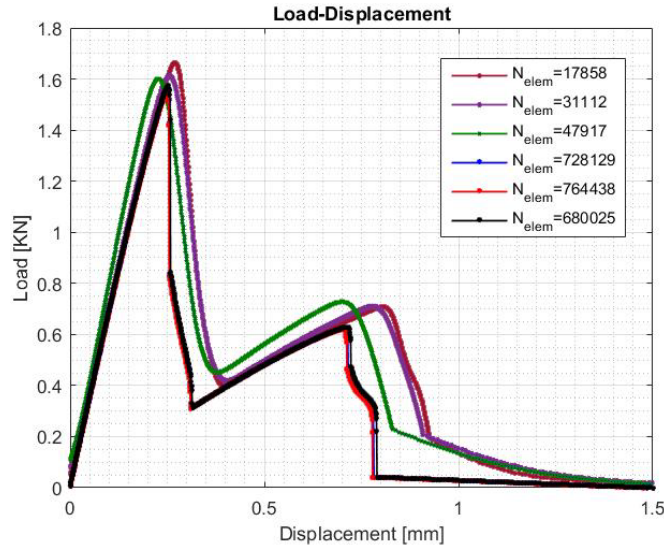


Figure 14. Comparison of the effect of the number of elements on the load–displacement behavior.

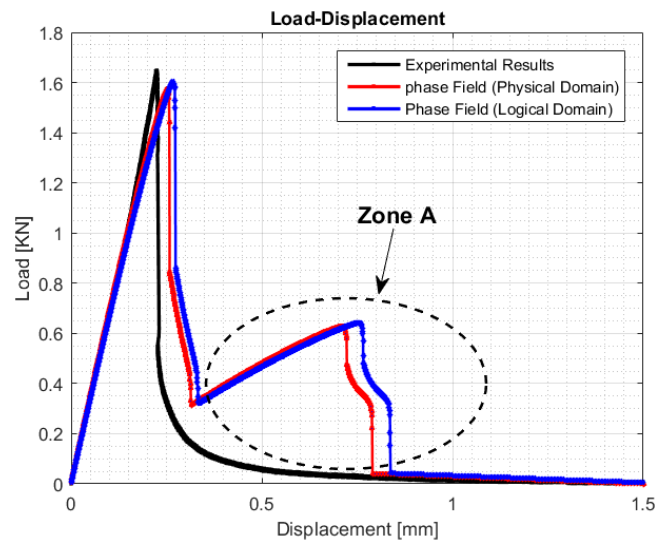


Figure 15. Comparison of the experimental results with the numerical results.

(porosity, weak paste–sand interfaces, notch irregularities). Moreover, the displacement is imposed ideally in the simulation, allowing the model to follow unstable branches of the energy path. By contrast, even under quasi-static conditions, the specimen and testing setup dissipate this instability, leading to a more gradual and continuous load decrease.

Finally, these results confirm that the phase-field model is capable of capturing highly brittle fracture phenomena, including elastic rebound behavior, even though certain features observed experimentally remain attenuated in the simulation.

The damage evolution in the structure is shown in Figure 16.

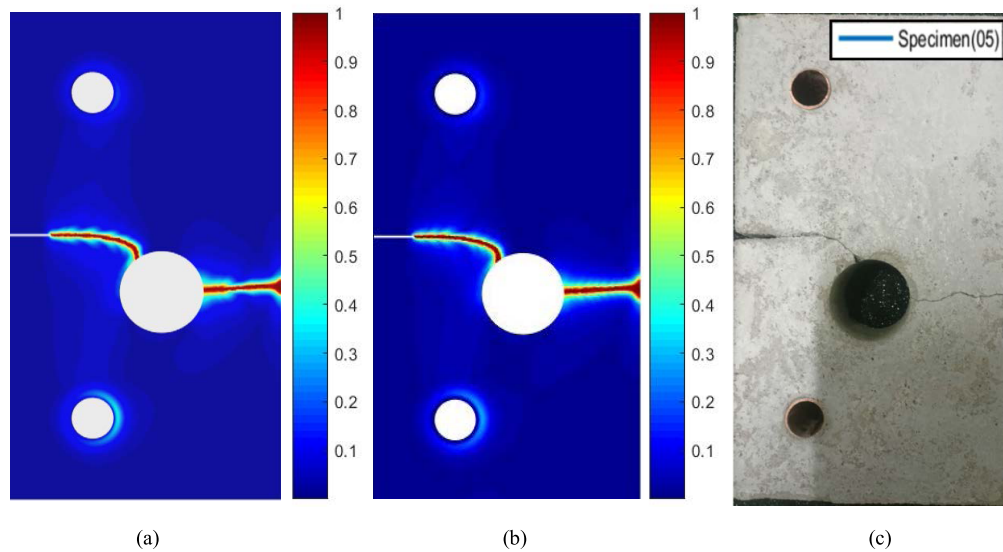


Figure 16. The evolution of the damage field in the structure (a) logical domain; (b) physical domain; (c) experimental result.

We can see that the crack starts in a straight line from the notch. It then continues along a curved path before joining the hole. At the imposed displacement $u_i = 0.73$ mm, a secondary crack is initiated from the hole and propagates in a straight line to the right-hand edge of the structure (total fracture of the specimen). We can see that the results of the numerical simulations in terms of cracking trajectories are in line with the results observed experimentally.

From a comparative point of view, there is a high degree of consistency between the results obtained in the logical and physical domains.

In order to better understand the effect of reinforcement on the holes where the loading is applied, whether in the logical domain through the bonding of copper tubes to these holes, or in the physical domain through the application of zero damage ($\phi = 0$) to the edges of these holes, a simulation was carried out where we added no reinforcement to these holes, and applied no conditions on the damage field at the edge of the holes where the loading is applied, i.e. the damage field is free throughout the structure.

The numerical and experimental results obtained are shown in Figure 17.

The results obtained in Figure 17(a) and (b) show qualitative agreement between numerical and experimental results. The structure was damaged on the holes where the loading was applied, confirming the validity and reliability of the experimental protocol adopted in the previous experiments in (Section 2) on the one hand, and the effectiveness of the numerical adaptation adopted to solve the problem of localizing damage at the edges of the loading zones in concrete mortar on the other.

6. Conclusion

The present work presents an experimental study and numerical modeling by the phase field model of the behavior of concrete mortar that contains predefined discontinuities, several points on have been addressed:

- The material parameters associated with the studied mortar were characterized in an integrated manner. The dynamic modulus of elasticity E_d and Poisson's ratio ν were monitored using ultrasonic testing at the ages of 7, 14, and 28 days, allowing repeated

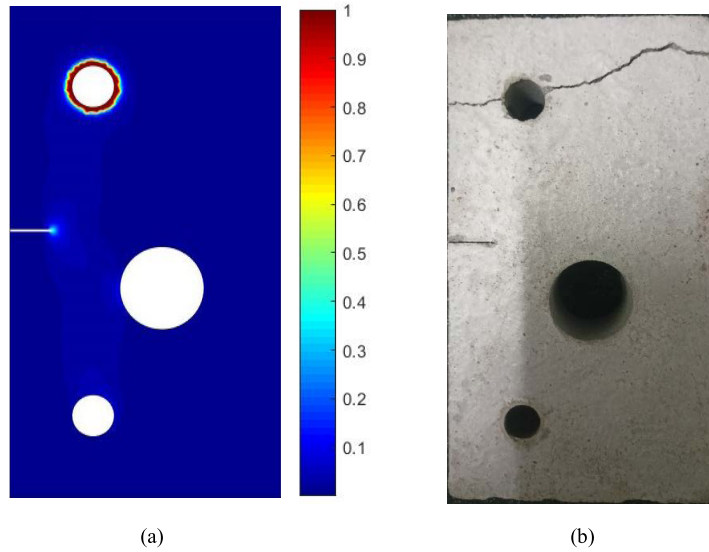


Figure 17. The evolution of the damage field in the structure (a) numerical result; (b) experimental result.

measurements on the same specimens. A three-point bending calibration enabled the establishment of a linear empirical relationship between the static and dynamic moduli ($E_s = a \times E_d + b$), specifically adapted to the investigated mortar. The fracture energy G_c was estimated from the load–displacement curves obtained in direct tensile tests and subsequently employed for numerical calibration.

- Quasi-static direct tensile tests were conducted on prismatic specimens containing a predefined crack and hole, using a servo-hydraulic testing machine. Three categories of specimens (7, 14, and 28 days) were tested to analyze the influence of age on the structural response.
- The phase-field method was implemented numerically within the framework of brittle fracture by the finite element method (FEM) through a MATLAB®-based computational code. The variational formulation was decomposed into two coupled equations (displacement and damage), solved using an explicit alternate minimization strategy. This implementation ensured enhanced numerical stability and reproducibility. The regularization parameter ℓ was physically justified by the sand granulometry, thereby establishing a direct link between the microstructure and the numerical model.
- The computational code was validated on a reference uniaxial tensile case and then applied to the experimental problem through the introduction of an original double-domain strategy: the logical domain, in which the complete experimental configuration was reproduced, and the physical domain, where the mechanical effect of the tubes was replaced by a simplified boundary condition ($\phi = 0$). This approach allowed numerical simplification while preserving physical representativeness. The phase-field method thus enabled the prediction of both crack propagation paths and load–displacement curves. A comparison was carried out between experimental and numerical results.

The following conclusions can be drawn from the results obtained:

- The mechanical properties of the mortar (elastic modulus, Poisson's ratio, stiffness) evolve with age, as evidenced by the characterization tests. This evolution is directly reflected in the direct tensile tests, where both strength and stiffness increase consistently with the characterization results.

- The experimental results highlight a progressive but non-linear increase in stiffness with age: a modest rise in the critical load between 7 and 14 days, followed by a pronounced increase between 14 and 28 days. These observations reflect a progressive densification of the microstructure.
- The phase-field damage model accurately reproduces the initiation and propagation of cracks in cement-based mortar, in overall agreement with the experimental observations. The numerical load–displacement curve, however, exhibits a rebound associated with the local resistance at the vicinity of the hole a phenomenon not observed experimentally, which can be attributed to the quasi-heterogeneous and highly brittle behavior of the mortar, characterized by paste–sand decohesion leading to a smoother global response. Numerically, dissipation nevertheless remains concentrated along the main crack.
- Instead of creating a logical domain, it would be sufficient to apply zero damage to the edges of the structure where displacement loading applies. This condition has the same effect as the previous one, since it avoids the localization (note that if the structure wanted to damage itself on these edges, this condition would not prevent it, since it would happen anyway) of the damage on these edges. The latter is easier to implement and is equivalent to the logical domain, which can become a difficult task for structures with more complex geometries.
- Due to the intrinsic nature of concrete as a heterogeneous composite material, characterized by its non-uniform distribution of various constituents and the complex interfaces that exist between these components, it becomes clear that these aspects play a crucial role in provoking not only the location of cracks, but also the subsequent paths through which these cracks propagate, as well as the ultimate mode of failure that may ensue.

Finally, this work opens up several avenues for future research:

- From an experimental perspective, an interesting direction would be the integration of local crack measurements (e.g., CMOD or DIC) in future experimental campaigns, in order to complement the global load–displacement measurements and achieve a more refined characterization of the direct tensile behavior.
- From a numerical perspective, a promising extension would be the implementation of an advanced arc-length type procedure, to better capture the snap-back phenomenon and analyze the unstable response of the material beyond the limitations of displacement control adopted in the present study.

Acknowledgements

The first author would like to express his sincere gratitude to Professor Hachi Brahim Elkhali for his valuable guidance on the phase-field damage model implemented in this work. He also wishes to thank Professor Zouari Bassem for his kind invitation to his laboratory at the National School of Engineers of Sfax and for his insightful advice on the experimental aspects. Finally, he extends his heartfelt thanks to Professor Mohamed Haboussi for his invitation to the LSPM Laboratory at Sorbonne Paris Nord University, France, and for his valuable recommendations regarding the structuring of this article.

Declaration of interests

The authors do not work for, advise, own shares in, or receive funds from any organization that could benefit from this article, and have declared no affiliations other than their research organizations.

Appendix A. Specimen preparation and detailed characterization of properties by ultrasonic tests

A.1. The steps for preparation of specimen

The specimens were prepared in the following steps:

- We prepared a wooden mold with the dimensions of the test specimen mentioned above.
- We ensured the proper clamping of the mold and eliminated any voids between the formwork walls using silicone. Then, we oiled the mold to facilitate de-molding.
- We mixed the sand and cement dry for 30 s, then added half of the water and mixed for 60 s. In the third step, we added the remaining water and mixed for another 90 s.
- The initial notch ($a_0 = 14$ mm) was directly created during casting by inserting a metallic plate of the corresponding dimensions into a dedicated slot in the mold. After filling the mixture and the beginning of the setting, the plate was carefully removed, and the mortar surface was leveled. This procedure ensured a clean and reproducible notch geometry, while avoiding any post-hardening cutting operations that could induce undesirable prestresses.
- We placed copper tubes on the mold so that they would stick to the inside surface of the small holes in the specimen after de-molding. The sufficiently high stiffness of the copper prevents the specimen from fracturing in the holes where the displacement loading is applied. This test is similar to the experimental PIED test proposed by Bazant et al. [96] and taken up by Ramtani et al. [97].
- We introduced the mixture into the formwork with vibration to distribute the grains evenly and ensure a compact fill.
- Once the mold has been filled, the surface is levelled using a ruler.
- The de-molding is carried out after 24 h.
- The test specimens were conserved at ambient temperature and relative moisture in the Laboratory of development in mechanic and materials (LDMM).

A.2. Detailed results of ultrasonic tests

This section of Annex A compiles the complete set of results obtained from the ultrasonic characterization of mortar specimens at the ages of 7, 14, and 28 days. The longitudinal wave

Table A1. Detailed results of ultrasonic velocities V_p , V_s , Poisson's ratio ν , and the moduli E_d and E_s for specimens at 7 days

	Longitudinal wave V_p (m/s) $\times 10^3$	Shear wave V_s (m/s) $\times 10^3$	Poisson's ratio ν	Average Poisson's ratio ν	Dynamic modulus of elasticity E_d (GPa)	Average dynamic modulus of elasticity E_s (GPa)	Average static modulus of elasticity E_s (GPa)	Average static modulus of elasticity E_s (GPa)
U-SP-07-D-01	4.9256	2.9851	0.2097		45.0308		0.4953388	
U-SP-07-D-02	4.9057	2.9695	0.2108		44.6001		0.4906011	
U-SP-07-D-03	4.8598	2.9617	0.2046		44.1372		0.4855092	
U-SP-07-D-04	4.8925	2.9931	0.2010		44.9404		0.4943444	
U-SP-07-D-05	4.8533	2.9773	0.1983	0.2062	44.3705	44.6653	0.4880755	0.4913188
U-SP-07-D-06	4.9389	3.0009	0.2074		45.4202		0.4996222	
U-SP-07-D-07	4.8404	2.9539	0.2033		43.8596		0.4824556	
U-SP-07-D-08	4.9189	2.9773	0.2109		44.8375		0.4932125	
U-SP-07-D-09	4.9123	2.9773	0.2097		44.7918		0.4927098	

Table A2. Detailed results of ultrasonic velocities V_p , V_s , Poisson's ratio ϑ , and the moduli E_d and E_s for specimens at 14 days

	Longitudinal wave V_p (m/s) $\times 10^3$	Shear wave V_s (m/s) $\times 10^3$	Poisson's ratio ϑ	Average Poisson's ratio ϑ	Dynamic modulus of elasticity E_d (GPa)	Average dynamic modulus of elasticity E_s (GPa)	Average static modulus of elasticity E_s (GPa)	Average static modulus of elasticity E_s (GPa)
U-SP-14-D-01	5.3139	3.2233	0.2089		52.4669		0.5771359	
U-SP-14-D-02	5.2984	3.2325	0.2036		52.5324		0.5778564	
U-SP-14-D-03	5.3216	3.2141	0.2129		52.3388		0.5757268	
U-SP-14-D-04	5.2907	3.2051	0.2101		51.9258		0.5711838	
U-SP-14-D-05	5.3061	3.2325	0.2049	0.2076	52.5922	52.4081	0.5785142	0.5706923
U-SP-14-D-06	5.3092	3.2233	0.2081		52.4319		0.5767509	
U-SP-14-D-07	5.3031	3.2417	0.2017		52.7511		0.5802621	
U-SP-14-D-08	5.2984	3.2141	0.2089		52.1665		0.5216650	
U-SP-14-D-09	5.3139	3.2233	0.2089		52.4669		0.5771359	

Table A3. Detailed results of ultrasonic velocities V_p , V_s , Poisson's ratio ϑ , and the moduli E_d and E_s for specimens at 28 days

	Longitudinal wave V_p (m/s) $\times 10^3$	Shear wave V_s (m/s) $\times 10^3$	Poisson's ratio ϑ	Average Poisson's ratio ϑ	Dynamic modulus of elasticity E_d (GPa)	Average dynamic modulus of elasticity E_s (GPa)	Average static modulus of elasticity E_s (GPa)	Average static modulus of elasticity E_s (GPa)
U-SP-28-D-01	6.2867	3.7965	0.2129		73.0323		0.8033553	
U-SP-28-D-02	6.2651	3.8093	0.2067		73.1464		0.8046104	
U-SP-28-D-03	6.2543	3.7965	0.2083		72.7479		0.8002269	
U-SP-28-D-04	6.2976	3.8093	0.2115		73.4352		0.8077872	
U-SP-28-D-05	6.2436	3.7965	0.2067	0.2100	72.6521	73.0781	0.7991731	0.8038076
U-SP-28-D-06	6.2759	3.8093	0.2083		73.2432		0.8056752	
U-SP-28-D-07	6.2651	3.7965	0.2098		72.8433		0.8012763	
U-SP-28-D-08	6.2543	3.7965	0.2083		72.7479		0.8002269	
U-SP-28-D-09	6.3415	3.8093	0.2177		73.8125		0.8119375	

velocities V_p and shear wave velocities V_s , the Poisson's ratio ϑ , as well as the dynamic modulus E_d and the static modulus E_s were determined for each specimen. Tables A1, A2, and A3 present the results corresponding to 7, 14, and 28 days, respectively.

References

- [1] S.-H. Chen, *Computational Geomechanics and Hydraulic Structures*, Springer: Singapore, 2019.
- [2] T.-T. Nguyen, D. Waldmann and T. Q. Bui, "Phase field simulation of early-age fracture in cement-based materials", *Int. J. Solids Struct.* **191** (2020), pp. 157–172.
- [3] M. F. Kaplan, "Crack propagation and the fracture of concrete", *ACI J. Proc.* **58** (1961), no. 11, pp. 591–610.
- [4] A. A. Griffith, "VI. The phenomena of rupture and flow in solids", *Philos. Trans. R. Soc. A* **221** (1921), no. 582–593, pp. 163–198.
- [5] E. Brühwiler, J. J. Broz and V. E. Saouma, "Fracture model evaluation of dam concrete", *J. Mater. Civ. Eng.* **3** (1991), no. 4, pp. 235–251.
- [6] X. Zhang and S. Xu, "A comparative study on five approaches to evaluate double-K fracture toughness parameters of concrete and size effect analysis", *Eng. Fract. Mech.* **78** (2011), no. 10, pp. 2115–2138.
- [7] S. Xu, Q. Li, Y. Wu, et al., "Influential factors for double-K fracture parameters analyzed by the round robin tests of RILEM TC265-TDK", *Mater. Struct.* **54** (2021), pp. 1–29.
- [8] E. N. Landis, "Micro-macro fracture relationships and acoustic emissions in concrete", *Int. J. Construction Building Materials* **13** (1999), no. 1, pp. 65–72.

- [9] S. Dai, X. Liu and K. Nawnit, "Experimental study on the fracture process zone characteristics in concrete utilizing DIC and AE methods", *Appl. Sci.* **9** (2019), no. 7, article no. 1346.
- [10] S. Y. Alam, J. Saliba and A. Loukili, "Fracture examination in concrete through combined digital image correlation and acoustic emission techniques", *Constr. Build. Mater.* **69** (2014), pp. 232–242.
- [11] S. Rouchier, G. Foray, N. Godin, M. Woloszyn and J. J. Roux, "Damage monitoring in fibre reinforced mortar by combined digital image correlation and acoustic emission", *Constr. Build. Mater.* **38** (2013), pp. 371–380.
- [12] S. Verbruggen, D. G. Aggelis, T. Tysmans and J. Wastiels, "Bending of beams externally reinforced with TRC and CFRP monitored by DIC and AE", *Compos. Struct.* **112** (2014), no. 1, pp. 113–121.
- [13] G. Sharma, S. Sharma and S. K. Sharma, "Fracture monitoring of steel and GFRP reinforced concrete beams using acoustic emission and digital image correlation techniques", *Struct. Concr.* **22** (2021), no. 4, pp. 1962–1976.
- [14] H. Zhang, H. Liu and H. Kuai, "Stress intensity factor analysis for multiple cracks in orthotropic steel decks rib-to-floorbeam weld details under vehicles loading", *Eng. Fail Anal.* **164** (2024), article no. 108705.
- [15] B. Fang, Z. Qian, Y. Song, et al., "Evaluation of early crack resistance performance of concrete mixed with ternary minerals using temperature stress testing machine (TSTM)", *J Clean Prod.* **465** (2024), article no. 142780.
- [16] J. Guan, Q. Li, Z. Wu, S. Zhao, W. Dong and S. Zhou, "Fracture parameters of site-cast dam and sieved concrete", *Mag. Concr. Res.* **68** (2016), no. 1, pp. 43–54.
- [17] Q. Li, J. Guan, Z. Wu, W. Dong and S. Zhou, "Equivalent maturity for ambient temperature effect on fracture parameters of site-casting dam concrete", *Constr. Build. Mater.* **120** (2016), pp. 293–308.
- [18] Q. Li, J. Guan, Z. Wu, W. Dong and S. Zhou, "Fracture behavior of site-casting dam concrete", *ACI Mater. J.* **112** (2015), no. 1, pp. 11–20.
- [19] F. Xu, Z. Wu, J. Zheng, Y. Zhao and K. Liu, "Crack extension resistance curve of concrete considering variation of FPZ length", *J. Mater. Civ. Eng.* **23** (2011), no. 5, pp. 703–710.
- [20] F. H. Wittmann, K. Rokugo, E. Brühwiler, H. Mihashi and P. Simonin, "Fracture energy and strain softening of concrete as determined by means of compact tension specimens", *Mater. Struct.* **21** (1988), pp. 21–32.
- [21] X. Chen, Y. Shao, L. Xu and C. Chen, "Experimental study on tensile behavior of cement paste, mortar and concrete under high strain rates", *J. Wuhan Univ. Technol. Mater. Sci. Ed.* **30** (2015), no. 6, pp. 1268–1273.
- [22] W. Zheng, A. K. H. Kwan and P. K. K. Lee, "Direct tension test of concrete", *ACI Mater. J.* **98** (2001), no. 1, pp. 63–71.
- [23] A. Mesbah, J. C. Morel, P. Walker and K. Ghavami, "Development of a direct tensile test for compacted earth blocks reinforced with natural fibers", *J. Mater. Civ. Eng.* **16** (2004), no. 1, pp. 95–98.
- [24] C. Rocco, G. V. Guinea, J. Planas and M. Elices, "Size effect and boundary conditions in the Brazilian test: theoretical analysis", *Mater. Struct.* **32** (1999), pp. 437–444.
- [25] T. S. Lok and J. R. Xiao, "Flexural strength assessment of steel fiber reinforced concrete", *J. Mater. Civ. Eng.* **11** (1999), no. 3, pp. 188–196.
- [26] G. Ruiz, M. Ortiz and A. Pandolfi, "Three-dimensional finite-element simulation of the dynamic Brazilian tests on concrete cylinders", *Int. J. Numer. Methods Eng.* **48** (2000), no. 7, pp. 963–994.
- [27] J. G. M. van Mier and M. R. A. van Vliet, "Uniaxial tension test for the determination of fracture parameters of concrete: state of the art", *Eng. Fract. Mech.* **69** (2002), no. 2, pp. 235–247.
- [28] H. W. Reinhardt, H. A. W. Cornelissen and D. A. Hordijk, "Tensile tests and failure analysis of concrete", *J. Struct. Eng.* **112** (1986), no. 11, pp. 2462–2477.
- [29] N. Olivier, B. C. La, P. Céline, R. Patrice and B. Gérard, "Experimental study of crack closure on heterogeneous quasi-brittle material", *J. Eng. Mech.* **141** (2015), no. 11, article no. 04015041.
- [30] F. Alhussainy, H. A. Hasan, M. N. Sheikh and M. N. S. Hadi, "A new method for direct tensile testing of concrete", *J. Test Eval.* **47** (2019), no. 2, pp. 704–718.
- [31] F. Alhussainy, H. A. Hasan, S. Rogic, M. Neaz Sheikh and M. N. S. Hadi, "Direct tensile testing of self-compacting concrete", *Constr. Build. Mater.* **112** (2016), pp. 903–906.
- [32] C. Wang and C. C. Sun, "A critical examination of three-point bending for determining Young's modulus", *Int. J. Pharm.* **629** (2022), article no. 122409.
- [33] A. S. Korolev, A. Kopp, D. Odnoburcev, et al., "Compressive and tensile elastic properties of concrete: empirical factors in span reinforced structures design", *Materials* **14** (2021), no. 24, article no. 7578.
- [34] A. R. Najibi, M. Ghafouri, G. R. Lashkaripour and M. R. Asef, "Empirical relations between strength and static and dynamic elastic properties of Asmari and Sarvak limestones, two main oil reservoirs in Iran", *J. Pet. Sci. Eng.* **126** (2015), pp. 78–82.
- [35] A. Boumiz, C. Vernet and F. C. Tenoudji, "Mechanical properties of cement pastes and mortars at early ages: evolution with time and degree of hydration", *Adv. Cem. Based Mater.* **3** (1996), no. 3, pp. 94–106.
- [36] L. P. Martin, E. A. Lindgren, M. Rosen and H. Sidhu, "Ultrasonic determination of elastic moduli in cement during hydrostatic loading to 1 GPa", *Mater. Sci. Eng. A* **279** (2000), no. 1, pp. 87–94.
- [37] J. Carette and S. Staquet, "Monitoring the setting process of mortars by ultrasonic P and S-wave transmission velocity measurement", *Constr. Build. Mater.* **94** (2015), pp. 196–208.

- [38] D. Kotsanis, P. Nomikos and D. Rozos, "Comparison of static and dynamic Young's modulus of prasinites", *Mater. Proc.* **5** (2021), no. 1, article no. 54.
- [39] K. Van Den Abeele, W. Desadeleer, G. De Schutter and M. Wevers, "Active and passive monitoring of the early hydration process in concrete using linear and nonlinear acoustics", *Cem. Concr. Res.* **39** (2009), no. 5, pp. 426–432.
- [40] N. Moës and T. Belytschko, "Extended finite element method for cohesive crack growth", *Eng. Fract. Mech.* **69** (2002), no. 7, pp. 813–833.
- [41] N. Moës, J. Dolbow and T. Belytschko, "A finite element method for crack growth without remeshing", *Int. J. Numer. Methods Eng.* **46** (1999), no. 1, pp. 131–150.
- [42] G. C. Sih and D.-Y. Tzou, "Three-dimensional transverse fatigue crack growth in rail head", *Theoret. Appl. Fract. Mech.* **1** (1984), no. 1, pp. 103–115.
- [43] L. Susmel, "The theory of critical distances: a review of its applications in fatigue", *Eng. Fract. Mech.* **75** (2008), no. 7, pp. 1706–1724.
- [44] L. Susmel and R. Tovo, "Estimating fatigue damage under variable amplitude multiaxial fatigue loading", *Fatigue Fract. Eng. Mater. Struct.* **34** (2011), no. 12, pp. 1053–1077.
- [45] L. Susmel and D. Taylor, "Fatigue design in the presence of stress concentrations", *J. Strain. Anal. Eng. Des.* **38** (2003), no. 5, pp. 443–452.
- [46] B. K. Hachi, Y. Belkacemi, S. Rechak, M. Haboussi and M. Taghite, "Fatigue growth prediction of elliptical cracks in welded joint structure: hybrid and energy density approach", *Theoret. Appl. Fract. Mech.* **54** (2010), no. 1, pp. 11–18.
- [47] G. A. Francfort and J.-J. Marigo, "Revisiting brittle fracture as an energy minimization problem", *J. Mech. Phys. Solids* **46** (1998), no. 8, pp. 1319–1342.
- [48] B. Bourdin, G. A. Francfort and J.-J. Marigo, "Numerical experiments in revisited brittle fracture", *J. Mech. Phys. Solids* **48** (2000), no. 4, pp. 797–826.
- [49] B. Bourdin, G. A. Francfort and J.-J. Marigo, "The variational approach to fracture", *J. Elast.* **91** (2008), pp. 5–148.
- [50] B. Bourdin, "Numerical implementation of the variational formulation for quasi-static brittle fracture", *Interface Free Bound.* **9** (2007), no. 3, pp. 411–430.
- [51] J. Lemaître and J. Dufailly, "Damage measurements", *Eng. Fract. Mech.* **28** (1987), no. 5–6, pp. 643–661.
- [52] C. Le Bellégo, J. F. Dubé, G. Pijaudier-Cabot and B. Gérard, "Calibration of nonlocal damage model from size effect tests", *Eur. J. Mech. A-Solids* **22** (2003), no. 1, pp. 33–46.
- [53] C. Iacono, L. J. Sluys and J. G. M. van Mier, "Estimation of model parameters in nonlocal damage theories by inverse analysis techniques", *Comput. Methods Appl. Mech. Eng.* **195** (2006), no. 52, pp. 7211–7222.
- [54] H. Amor, J.-J. Marigo and C. Maurini, "Regularized formulation of the variational brittle fracture with unilateral contact: numerical experiments", *J. Mech. Phys. Solids* **57** (2009), no. 8, pp. 1209–1229.
- [55] K. Pham, H. Amor, J.-J. Marigo and C. Maurini, "Gradient damage models and their use to approximate brittle fracture", *Int. J. Damage Mech.* **20** (2011), no. 4, pp. 618–652.
- [56] E. Tanné, T. Li, B. Bourdin, J.-J. Marigo and C. Maurini, "Crack nucleation in variational phase-field models of brittle fracture", *J. Mech. Phys. Solids* **110** (2018), pp. 80–99.
- [57] H. Q. Nguyen, B. V. Tran, B. A. Le and T. T. Nguyen, "On the choice of a phase field model for describing fracture behavior of concrete", *Int. J. Comput. Mater. Sci. Eng.* **13** (2024), no. 01, article no. 2350016.
- [58] H. Li, Y. Huang, Z. Yang, K. Yu and Q. M. Li, "3D meso-scale fracture modelling of concrete with random aggregates using a phase-field regularized cohesive zone model", *Int. J. Solids Struct.* **256** (2022), article no. 111960.
- [59] P. Grassl, H. S. Wong and N. R. Buenfeld, "Influence of aggregate size and volume fraction on shrinkage induced micro-cracking of concrete and mortar", *Cem. Concr. Res.* **40** (2010), no. 1, pp. 85–93.
- [60] C. Miehe, F. Welschinger and M. Hofacker, "Thermodynamically consistent phase-field models of fracture: variational principles and multi-field FE implementations", *Int. J. Numer. Methods Eng.* **83** (2010), no. 10, pp. 1273–1311.
- [61] P. Farrell and C. Maurini, "Linear and nonlinear solvers for variational phase-field models of brittle fracture", *Int. J. Numer. Methods Eng.* **109** (2017), no. 5, pp. 648–667.
- [62] G. Pijaudier-Cabot and Z. P. Bazant, "Nonlocal damage theory", *J. Eng. Mech.* **113** (1987), no. 10, pp. 1512–1533.
- [63] Z. P. Bazant and M. Jirásek, "Nonlocal integral formulations of plasticity and damage: survey of progress", *J. Eng. Mech.* **128** (2002), no. 11, pp. 1119–1149.
- [64] N. Moës, C. Stolz, P. Bernard and N. Chevaugeon, "A level set based model for damage growth: the thick level set approach", *Int. J. Numer. Methods Eng.* **86** (2011), no. 3, pp. 358–380.
- [65] P. E. Bernard, N. Moës and N. Chevaugeon, "Damage growth modeling using the thick level set (TLS) approach: efficient discretization for quasi-static loadings", *Comput. Methods Appl. Mech. Eng.* **233–236** (2012), pp. 11–27.
- [66] A. Salzman, N. Moës and N. Chevaugeon, "On use of the thick level set method in 3D quasi-static crack simulation of quasi-brittle material", *Int. J. Fract.* **202** (2016), no. 1, pp. 21–49.

- [67] N. Moës and N. Chevaugeon, “Lipschitz regularization for softening material models: the Lip-field approach”, *C. R. Méc.* **349** (2021), no. 2, pp. 415–434.
- [68] N. Chevaugeon and N. Moës, “Lipschitz regularization for fracture: the Lip-field approach”, *Comput. Methods Appl. Mech. Eng.* **402** (2022), article no. 115644.
- [69] N. Moës, B. Lé, N. Chevaugeon and J.-F. Remacle, “Phase-field and lip-field approaches for fracture with extreme mesh deformation (X-Mesh): a one-dimensional study”, *C. R. Méc.* **353** (2025), no. G1, pp. 1027–1051.
- [70] B. Bourdin, C. Chukwudozie and K. Yoshioka, “A variational approach to the numerical simulation of hydraulic fracturing”, in *SPE Annual Technical Conference and Exhibition*, SPE: San Antonio, TX, 2012. SPE-159154.
- [71] S. Lee, M. F. Wheeler and T. Wick, “Pressure and fluid-driven fracture propagation in porous media using an adaptive finite element phase field model”, *Comput. Methods Appl. Mech. Eng.* **305** (2016), pp. 111–132.
- [72] C. Miehe, M. Hofacker and F. Welschinger, “A phase field model for rate-independent crack propagation: robust algorithmic implementation based on operator splits”, *Comput. Methods Appl. Mech. Eng.* **199** (2010), no. 45–48, pp. 2765–2778.
- [73] J. M. Sargado, E. Keilegavlen, I. Berre and J. M. Nordbotten, “High-accuracy phase-field models for brittle fracture based on a new family of degradation functions”, *J. Mech. Phys. Solids* **111** (2018), pp. 458–489.
- [74] J.-Y. Wu, “A unified phase-field theory for the mechanics of damage and quasi-brittle failure”, *J. Mech. Phys. Solids* **103** (2017), pp. 72–99.
- [75] Y. Kriaa, H. Hentati and B. Zouari, “Applying the phase-field approach for brittle fracture prediction: numerical implementation and experimental validation”, *Mech. Adv. Mater. Struct.* **29** (2022), no. 6, pp. 828–839.
- [76] R. Piska, K. Sivasdas, K. Boyina, et al., “Recent trends in computational damage models: an overview”, *Theoret. Appl. Fract. Mech.* **132** (2024), article no. 104494.
- [77] Y. Yu, C. Hou, T. Rabczuk and M. Zhao, “A simple and efficient solution scheme of coupling method between phase field regularized cohesive zone model and linear elastic model for fracture”, *Theoret. Appl. Fract. Mech.* **134** (2024), article no. 104696.
- [78] B. E. Hachi, M. Boudouh, S. Ramtani, M. Haboussi and H. Liu, “Enhanced brittle fracture modeling in heterogeneous materials: a variational phase field approach integrating XFEM and Level-Set methods”, *Int. J. Comput. Methods* **22** (2025), no. 7, article no. 2550003.
- [79] M. Krauß and K. Hariri, “Determination of initial degree of hydration for improvement of early-age properties of concrete using ultrasonic wave propagation”, *Cem. Concr. Compos.* **28** (2006), no. 4, pp. 299–306.
- [80] A. I. Marques, J. Morais, P. Morais, et al., “Modulus of elasticity of mortars: Static and dynamic analyses”, *Constr. Build. Mater.* **232** (2020), article no. 117216.
- [81] W. de A. Thomaz, D. Y. Miyaji and E. Possan, “Comparative study of dynamic and static Young’s modulus of concrete containing basaltic aggregates”, *Constr. Mater.* **15** (2021), article no. e00645.
- [82] M. R. Asef and M. Farokhrouz, “A semi-empirical relation between static and dynamic elastic modulus”, *J. Pet. Sci. Eng.* **157** (2017), pp. 359–363.
- [83] F. D. Lydon and R. V. Balendran, “Some observations on elastic properties of plain concrete”, *Cem. Concr. Res.* **16** (1986), no. 3, pp. 314–324.
- [84] J. Lee and M. M. Lopez, “An experimental study on fracture energy of plain concrete”, *Int. J. Concr. Struct. Mater.* **8** (2014), pp. 129–139.
- [85] G. Giaccio, C. Rocco and R. Zerbino, “The fracture energy (GF) of high-strength concretes”, *Mater. Struct.* **26** (1993), pp. 381–386.
- [86] RILEM TC50 FMC, “Determination of the fracture energy of mortar and concrete by means of three-point bend tests on notched beams”, *Mater. Struct.* **18** (1985), no. 4, pp. 287–290.
- [87] S. Khalilpour, E. Baniasad and M. Dehestani, “A review on concrete fracture energy and effective parameters”, *Cem. Concr. Res.* **120** (2019), pp. 294–321.
- [88] G. A. Francfort and J.-J. Marigo, “Stable damage evolution in a brittle continuous medium”, *Eur. J. Mech. A-Solids* **12** (1993), pp. 149–189.
- [89] G. Francfort and J.-J. Marigo, “Vers une théorie énergétique de la rupture fragile”, *C. R. Méc.* **330** (2002), no. 4, pp. 225–233.
- [90] H. Amor, *Approche variationnelle des lois de Griffith et de Paris via des modèles non-locaux d’endommagement : étude théorique et mise en oeuvre numérique*, Thèse de doctorat Modélisation et simulation, Université Paris-Nord - Paris XIII, 2008. Online at <https://tel.archives-ouvertes.fr/tel-00352989> (accessed on January 14, 2009).
- [91] L. Ambrosio and V. M. Tortorelli, “Approximation of functional depending on jumps by elliptic functional via t -convergence”, *Commun. Pure Appl. Math.* **43** (1990), no. 8, pp. 999–1036.
- [92] D. B. Mumford and J. Shah, “Optimal approximations by piecewise smooth functions and associated variational problems”, *Commun. Pure Appl. Math.* **42** (1989), no. 7, pp. 577–685.
- [93] M. J. Borden, *Isogeometric analysis of phase-field models for dynamic brittle and ductile fracture*, PhD thesis, The University of Texas at Austin, 2012.

- [94] M. J. Borden, C. V. Verhoosel, M. A. Scott, T. J. R. Hughes and C. M. Landis, “A phase-field description of dynamic brittle fracture”, *Comput. Methods Appl. Mech. Eng.* **217** (2012), pp. 77–95.
- [95] M. Dhahri, *Etude de la rupture et de l'endommagement par choc thermique des matériaux fragiles et de l'influence des effets dynamiques à partir de l'approche champ de phase*, Thèse de doctorat, Matériaux et structures en mécanique [physics.class-ph], Université Paris-Nord - Paris XIII; Université de Tunis El Manar, 2022. Online at <https://theses.hal.science/tel-03937783> (accessed on January 13, 2023).
- [96] Z. P. Bažant and G. Pijaudier-Cabot, “Measurement of characteristic length of nonlocal continuum”, *J. Eng. Mech.* **115** (1989), no. 4, pp. 755–767.
- [97] S. Ramtani, Y. Berthaud and J. Mazars, “Orthotropic behavior of concrete with directional aspects: modelling and experiments”, *Nucl. Eng. Des.* **133** (1992), no. 1, pp. 97–111.